Thermodynamic size control in curvature-frustrated tubules: Self-limitation with open boundaries

Botond Tyukodi,[†] Farzaneh Mohajerani,[†] Douglas M. Hall,[‡] Gregory M. Grason,[*,‡] and Michael F. Hagan[*,†]

[†]*Martin Fisher School of Physics, Brandeis University, Waltham, Massachusetts 02454, USA*

[‡]*Department of Polymer Science and Engineering, University of Massachusetts, Amherst, Massachusetts 01003, USA*

E-mail: grason@mail.pse.umass.edu; hagan@brandeis.edu

Abstract

We use computational modeling to investigate the assembly thermodynamics of a particle-based model for geometrically frustrated assembly, in which the local packing geometry of subunits is incompatible with uniform, strain-free large-scale assembly. The model considers discrete triangular subunits that drive assembly towards a closed, hexagonal-ordered tubule, but have geometries that locally favor negative Gaussian curvature. We use dynamical Monte Carlo simulations and enhanced sampling methods to compute the free energy landscape and corresponding self-assembly behavior as a function of experimentally accessible parameters that control assembly driving forces and the magnitude of frustration. The results determine the parameter range where finite-temperature self-limiting assembly occurs, in which the equilibrium assembly size

distribution is sharply peaked around a well-defined finite size. The simulations also identify two mechanisms by which the system can escape frustration and assemble to unlimited size, and determine the particle-scale properties of subunits that suppress unbounded growth.

Keywords: self-limited assembly, geometric frustration, free energy calculations, programmable assembly, dynamical Monte Carlo, umbrella sampling, parallel tempering

The self-assembly of subunits into large, but finite-size, superstructures plays a central role in the functionalities, pathogenesis, and organization of biological systems (e.g. viral capsids,[1–8] bacterial microcompartments[9–14] and other shelled cell organelles[15–18]), and is becoming a route to design nanostructured assemblies for technological applications .[19–29] In contrast, most subunits with cohesive interactions typically undergo thermodynamically unlimited assembly, for example into a crystal. In these examples self-limitation arises through 'curvature control', meaning that subunits assemble with a preferred curvature that drives the structure to close upon itself, leaving no boundary for additional subunit association.

In a second class of self-limited, *open-boundary* structures, self-assembly terminates at a well-defined equilibrium size without self-closure, leaving free boundaries at which subunits can readily exchange with the bulk. Possible biological examples include fiber bundles with well-defined diameters formed by sickle-cell hemoglobin or fibrin[30,31]. Recently, it has been theoretically proposed that self-limited open-boundary assembly can be achieved through 'geometric frustration' (GF), in which the preferred local packing of subunits is incompatible with their preferred large-scale assembly structure.[32–34] This incompatibility leads to a misfit strain energy that grows super-extensively with assembly size until it overwhelms the cohesive interactions that drive assembly, leading to a finite equilibrium size. For example, theory showed that twisted fiber bundles can have self-limited diameters because the preferred skew of the filament-filament interactions is incompatible with the preferred 2D lattice packing

in the cross-section[35–40], while the growth of intra-membrane stretching with lateral size of 2D crystalline assemblies with incompatible Gaussian curvature can lead to ribbons of self-limited widths[41–47]. In these and other examples, it is predicted that the range of self-limitation is delimited by mechanisms of 'frustration escape', whereby defects or elastic distortions effectively screen the super-extensive frustration cost and permit unlimited (bulk) assembly.[32,34,48]

The mechanism of self-limitation by GF is fundamentally distinct from more common and widely known examples of self-limited amphiphillic assembly into finite-size micelles.[49] While assembly may strain molecules in micelles, such strains are intra-molecular (i.e. chain stretching), and thus the ultimate range of finite diameters is limited by the subunit dimensions (e.g. length of a surfactant). In contrast, GF leads to *gradients* in inter-subunit strain that propagate throughout the assembly, and vary in magnitude with the finite size.[32,34] Thus, GF-driven equilibrium finite sizes can in principle extend orders of magnitude beyond the size of subunits or their interaction range.[8]

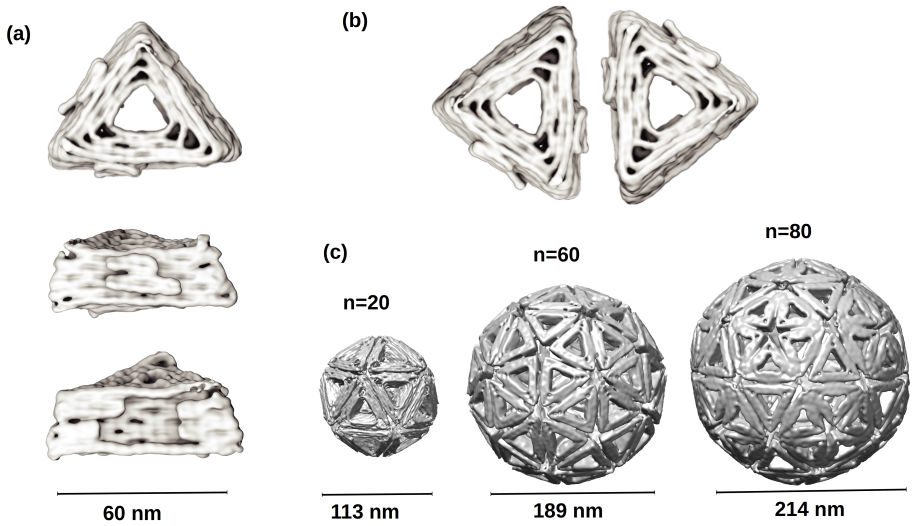

Figure 1: Cryogenic electron microscopy images of DNA origami subunits and capsids that they assemble into. **(a)** Top view and two side views of subunits. **(b)** Two subunits binding to each other. The subunits assemble along their edges through shape-complementary interactions driven by blunt-end DNA base stacking.[19] **(c)** Icosahedral capsids composed of $n = 20$, 60 and 80 subunits. The target structure is defined by the bevel angles of subunit edges. The images in (a)-(c) were provided by C. Sigl.

Understanding and engineering the effects of GF on physical assemblies requires connecting the mechanisms and range of strain accumulations, and complex modes of frustration escape, to particle-scale properties of the misfit building blocks. However, our current understanding of GF-limited assembly derives primarily from continuum elastic descriptions of the ground-state energetics, with strong assumptions about the symmetries of aggregates. While these descriptions establish that in idealized ground states stress buildup could overwhelm gains of additional subunit binding, such stresses may instead lead to fragmented and uncontrolled morphologies. It thus remains unknown when such models represent the thermodynamically relevant aggregates, whether finite-temperature fluctuations enhance or suppress self-limitation, whether low-symmetry aggregates with defects enable escape from self-limitation, and what is the physical limit of assembly sizes and conditions where a given system exhibits self-limitation.

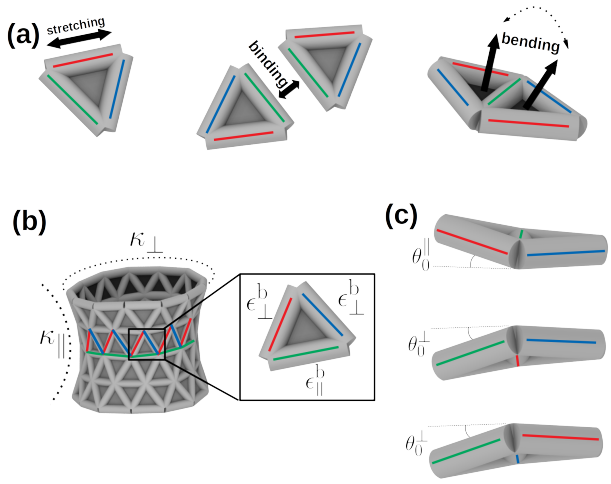

Figure 2: **(a)** Model energies account for edge stretching, binding of subunits, and bending across bonds. **(b),(c)** Subunits have three edge types and each type can only bind to its own kind. Two of the types (marked with red and blue lines) have the same binding energy $\epsilon_\perp^b$ and preferred dihedrals $\theta_0^\perp$ which set the concave curvature $\kappa_\perp$. The third type (green lines) has a different binding energy $\epsilon_\parallel^b$ and its preferred dihedral $\theta_0^\parallel$ sets the convex curvature $\kappa_\parallel < 0$.

In this paper, we study a discrete particle model of GF tubule assembly by combining Monte Carlo simulations with enhanced sampling to determine the equilibrium phase

diagram of a GF system, accounting for finite temperature and concentration and without assumptions about assembly pathways, subunit packing geometry, or defects. While we focus on a particular example, the implications of GF for assembly studied here are generic, and analogous arguments can be made for systems with diverse sources of GF.[8,32,33] Our model can be realized in experiments based on DNA origami (e.g. Fig. 1) or polymer hydrogel subunits,[19,20,50–52] and we identify experimental control parameters that enable tuning the finite equilibrium size. Thus, our computational predictions can be directly tested by experiments. Further, our results identify bounds on self-limited assembly, beyond which factors not accounted for in continuum descriptions allow GFA systems to escape into unlimited assembly. However, we also identify design strategies to suppress frustration escape, thereby increasing the parameter range over which self-limited assembly can be achieved.

Results and discussion

Inspired by DNA origami experiments[19] that target spherical capsids (Fig. 1) and helical tubules[53] , we consider a minimal model of GF assembly: identical equilateral triangular subunits that assemble along their edges to form an elastic sheet curled into a tubular structure (Fig. 2).

The subunit edge shapes favor *concave* (i.e. self-closing) curvature $\kappa_\perp > 0$ in the hoop direction, but unlike cylindrical tubular assemblies,[50,54] simultaneously favor *convex* curvature $\kappa_\parallel < 0$ in the other. Thus, this preferred geometry targets a negative Gaussian curvature $K_\mathrm{G} = \kappa_\perp \kappa_\parallel < 0$, which is incompatible with the uniform triangular lattice favored by the equilateral subunit geometry. Assuming morphologies to be axisymmetric and defect-free, an assumption that we test below, assemblies are catenoid-like tubules ('trumpets'), whose size and shape is determined by a balance of stretching and bending elasticity.

Frustration is driven by negatively-curved splaying at both free ends of a trumpet, which leads to a stretching strain of self-closing hoops of subunits that grows in extent along

the axial length. Assuming all other parameters to be fixed, longer trumpets experience a larger hoop strain at their ends, and thus are more frustrated. Assuming constant principal curvatures throughout the trumpet surface, which we show holds in the short trumpet limit, the radial deflection of the sheet at either end of the trumpet is $\delta \approx (1/8)\kappa_{\parallel} L^2$. The corresponding hoop strain, arising from the increase in the hoop diameter, is $\varepsilon = \delta/R_{\perp} \approx (1/8)\kappa_{\parallel}\kappa_{\perp} L^2$ where $R_{\perp} = 1/\kappa_{\perp}$ is the trumpet radius at its central hoop. Thus, the (hoop) strain grows with trumpet length L as $\varepsilon \sim K_{\mathrm{G}} L^2$. Defining Y as the elastic stretching modulus, the corresponding elastic energy density grows as $e(L) \sim Y\varepsilon^2 \approx Y K_{\mathrm{G}}^2 L^4$, and the total elastic energy as $E(L) \approx Y K_{\mathrm{G}}^2 L^5/\kappa_{\perp}$. Notably this scaling is consistent with the known Föppl von Kárman relation between Gaussian curvature and stress gradients in elastic sheets[32] .

Zero-temperature continuum theory arguments, as considered previously,[8,41,42] present a simplified picture of the assembly thermodynamics, under the strong assumption of axisymmetry. For sufficiently short trumpets, the cumulative hoop stretching cost is much smaller than the unbending cost to flatten the axial curvature. Hence, short trumpets adopt nearly the target Gaussian curvature, and the free energy as a function of length is given by the stretching and edge contributions, $F(L) \sim 2\pi\kappa_{\perp}^{-1}\big(Y K_{\mathrm{G}}^2 L^5 + 2\Lambda\big)$ with Λ the line energy accounting for unsatisfied subunit interactions at the trumpet ends. An equilibrium self-limited length L_* in the canonical ensemble requires a minimumShe in the *per-subunit* free energy $\sim F/(\kappa_{\perp}^{-1} L)$,[8] which is given by $L_* \cong \big[\Lambda/(Y K_{\mathrm{G}}^2)\big]^{1/5}$. Unlike the aforementioned bundle and ribbon assemblies which undergo unfrustrated, unlimited growth in one direction, the simultaneously self-closing hoop and frustration-limited length of a trumpet implies self-limitation with a finite *mass*, as we demonstrate below.

As edge tension increases, the optimal length grows, until the hoop stretching cost per unit area overwhelms the cost of unbending (flattening) in the axial direction, $\approx B\kappa_{\parallel}^2/2$, with B the bending modulus. Since the energy density cost of flattening $\sim B\kappa_{\parallel}^2$ is length independent and the energy density of stretching $\sim Y K_{\mathrm{G}}^2 L^4$, the former term dominates in

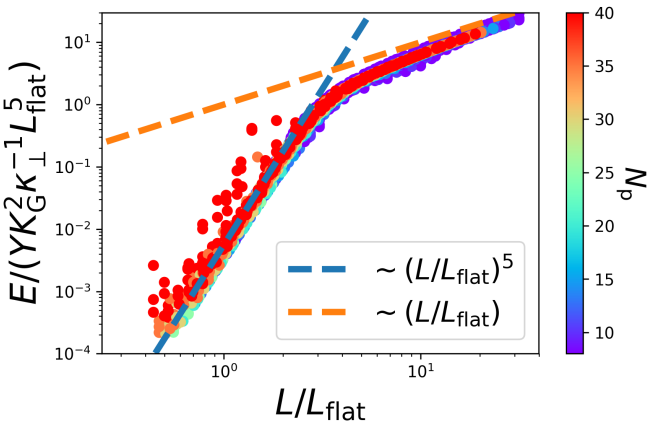

Figure 3: Scaling collapse of trumpet elastic energies. The ground state energies of trumpets in the discrete particle model are shown as a function of their lengths, scaled as suggested by the arguments described in the text. The color code indicates different trumpet diameters, with $2N_\mathrm{p}$ subunits in each ring. Each point represents an individual trumpet with given diameter, length, stretching and bending modulus. There are a total of 1872 points on the plot, corresponding to trumpets with lengths $L \in [2, 40]$ rings, $N_\mathrm{p} \in [8, 40]$ subunits, stretching moduli $\epsilon_\mathrm{s} \in [50, 500]$, and bending moduli $\kappa_\mathrm{b} \in [50, 500]$. The microscopic moduli ϵ_s and κ_b were mapped to the continuum moduli following Ref.[55] as $Y = \left(\sqrt{3}/2\right)\epsilon_\mathrm{s}$ and $B = \left(2/\sqrt{3}\right)\kappa_\mathrm{b}$. The trumpet energies were computed by reducing the system temperature to zero at fixed topology of the structure as described in the text.

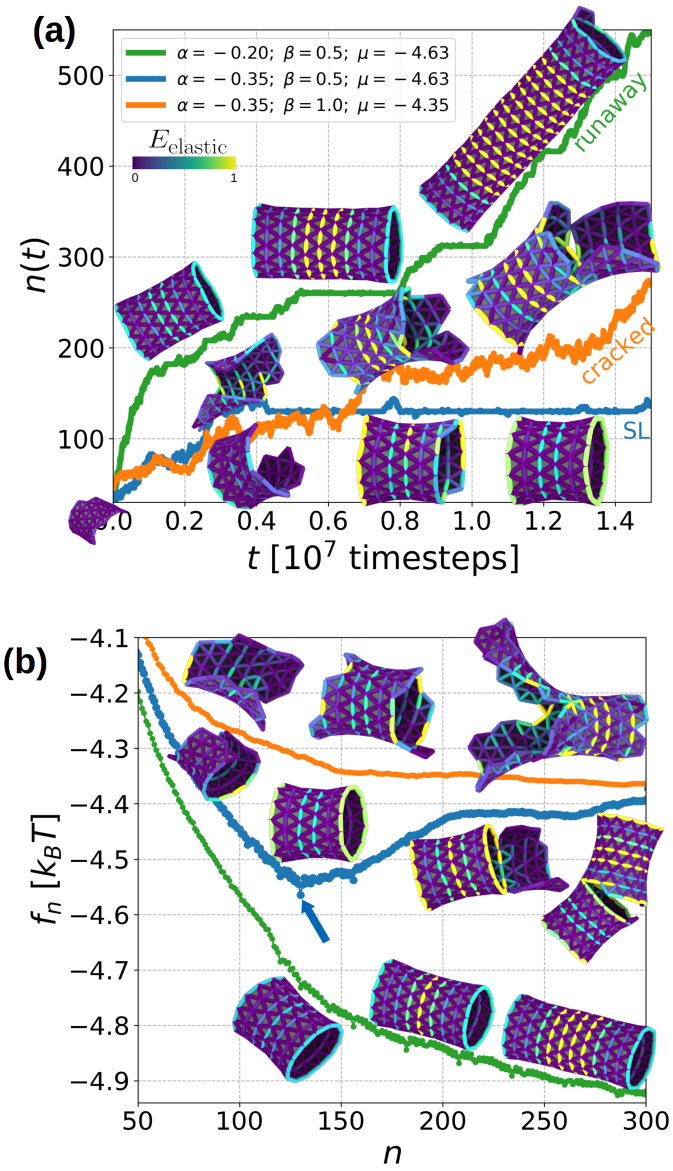

Figure 4: **(a)** Cluster size as a function of time for dynamical simulations that respectively illustrate the three classes of assembly behaviors: cracked, runaway, and self-limited (with optimal size $n_* = 130$). Snapshots generated with Ovito[56] along each trajectory are shown, with edges color-coded by their ground-state elastic energies. The curvature anisotropy $\alpha = \kappa_\parallel/\kappa_\perp$, binding anisotropy $\beta = \epsilon^{\rm b}_\parallel/\epsilon^{\rm b}_\perp$, and chemical potential μ values are shown in the legend. **(b)** Per-subunit free energy profiles corresponding to the dynamical simulations in (a), obtained by umbrella sampling with replica exchange between 36 ensembles with different chemical potentials, temperatures, and bias potentials. The regularly spaced local minima correspond to full ring closures. The arrow indicates the global minimum for the middle profile ($\alpha = -0.35, \beta = 0.5$). The other profiles do not exhibit global minima. For all 3 systems, the elastic parameters are $\epsilon_{\rm s} = 150 k_{\rm B}T/l_0^2$ and $\kappa_{\rm b} = 300 k_{\rm B}T$; the mean binding energy is $\langle \epsilon_{\rm b} \rangle = (2\epsilon^{\rm b}_\perp + \epsilon^{\rm b}_\parallel)/3 = -6.5 k_{\rm B}T$; and the hoop curvature is $\kappa_\perp \approx 2\pi/(N_{\rm p} l_0)$, which favors $2N_{\rm p} = 26$ subunits in a ring.

the small L regime, and assemblies maintain a constant negative curvature. As the length grows, however, the stretching cost overwhelms bending costs when $B\kappa_{\parallel}^2 \approx Y K_{\mathrm{G}}^2 L^4$. This crossover from stretching- to bending-dominated costs defines a characteristic length scale $L_{\mathrm{flat}} \sim \left(B/Y\kappa_{\perp}^2\right)^{1/4}$ beyond which the trumpet interior 'flattens' at the expense of bending energy due to deviations from the preferred curvature.[8] However, beyond this anticipated flattening of weakly frustrated assemblies, it remains unclear if and under what conditions the axisymmetric morphologies considered by these continuum arguments represent the relevant states that self-assemble when symmetries are unconstrained.

To investigate how the combined effects of finite temperature fluctuations as well as low-symmetry and defective morphologies alter this self-limiting assembly scenario, we adapt a discrete subunit model previously developed for elastic membranes[55] and icosahedral shell self-assembly.[57–61] This approach does not explicitly resolve the small-scale diffusive motions of subunits, and thus facilitates the sampling of competing morphologies required to identify equilibrium self-limited states at finite temperature. The model describes a growing elastic sheet comprised of identical triangular subunits, which have three distinct edge types (Fig. 2a). Here, we consider subunits that bind to each other only along like edges. This choice is based on the principle that a well-designed assembly process has a unique ground state corresponding to the target geometry. To specify a particular local curvature geometry as the lowest energy target state (i.e. with a particular preferred local curvatures) each edge must bind to a specific edge on the neighboring subunit, aligning distinct dihedral angles in particular directions relative to axial and coaxial direction of trumpets (see SI Fig. S12). In the DNA origami experiments on tubule assembly that inspire our model, such edge specificity was insured by shape-complementary binding of blunt-end DNA-DNA interactions along each edge.[53]

The stability of rings is adjusted via the intra-ring binding energy $\epsilon_{\perp}^{\mathrm{b}}$, which is the subunit-subunit binding energy along the circumference. The inter-ring binding energy, i.e. the binding strength along the axial direction, is $\epsilon_{\parallel}^{\mathrm{b}}$. In the following, we fix the subunit compliance

and the mean binding energy, and vary two dimensionless ratios: i) the curvature anisotropy: $\alpha = \kappa_{\parallel}/\kappa_{\perp}$ and ii) binding anisotropy $\beta = \epsilon_{\parallel}^{\mathrm{b}}/\epsilon_{\perp}^{\mathrm{b}}$.

To test the correspondence between elastic energetics of trumpets in our discrete model to the continuum arguments described above, first we consider the zero-temperature energy minima of pre-assembled trumpets of different lengths, preferred diameters, and elastic moduli in Fig. 3. These structures were slowly quenched to $T = 0$ while prohibiting subunit addition or removal or defect formation, so that their topologies remained fixed during quenching. Their elastic energy as a function of length was then measured in the final, $T = 0$ state. Fig. 3 shows the results, with lengths scaled by the predicted flattening crossover size L_{flat} and energies scaled by the flattening energy cost $\approx Y K_{\mathrm{G}}^2 L^5/\kappa_{\perp}$. We observe excellent scaling collapse over a wide range of parameters, and the clear emergence of two regimes: at small lengths a superextensive cost of the elastic frustration, where $E \sim L^5$, and at large lengths a convergence to an extensive energy where $E \sim L$. This crossover is a fingerprint of flattening, and demonstrates that the continuum arguments presented above apply to our discrete model *in the zero temperature limit*.

We next evaluate assembly dynamics at finite temperatures. Fig. 4a shows example trajectories from dynamical simulations for three parameter sets, which qualitatively illustrate the three structural categories that we observe. At small curvature anisotropies (green line, labeled 'runaway'), i.e. approaching an unfrustrated cylinder, $\alpha \to 0$, small structures form with the negative Gaussian curvature favored by individual subunits. However, beyond a certain length the curvature-driven stresses are screened and the trumpet interior 'flattens', pushing the negative Gaussian curvature to a narrow zone near the free ends. Consequently the length-dependent elastic energy of deformation approaches an extensive bulk term associated with interior flattening plus a length-independent boundary term, and the trumpet undergoes unbounded longitudinal growth. At large curvature or binding anisotropies (orange line, 'cracked'), the trumpets either fail to close or else crack, leading to disorganized (e.g. branched) but unbounded growth. However, we observe self-limited

growth at an intermediate range of curvature anisotropy (blue line, 'self-limited'). Structures have a catenoid-like geometry (negatively-curved regions of constant positive mean curvature unduloids), and after growing to final size n_* exhibit only small thermal fluctuations in length.

To test whether dynamical simulations correspond to equilibrium phenomena, Fig. 4b shows the per-subunit interaction free energies f_n for the three systems introduced in Fig. 4a. The free energies of the runaway and cracked structures monotonically decrease with n, although they asymptotically flatten for large n since the per-subunit edge energy diminishes as $1/n$. While both structures escape self-limitation, they do so via very different mechanisms. According to the continuum theory arguments above, for runaway trumpets the elastic energy is screened beyond a *penetration length* $L_{\rm flat} \sim \kappa_\perp^{-1/2}$, and flattening of the trumpet interior becomes energetically favorable. The elastic (bending) energy cost of flattening is extensive in n and thus avoids the super-extensive cost of progressive stretching of outer hoops. In contrast, the cracks in high-curvature anisotropy structures incur line energy costs (from missing bonds), but locally release elastic energy. The elastic and cohesive energies of longitudinal cracks grow with their length, and hence, beyond the size at which cracks are stable, the trumpet energy grows extensively. Since either elastic flattening or crack formation preempt the self-limiting compromise between stretching and edge energy, they do not exhibit minima in f_n.

In contrast, the self-limited structure (blue line in Fig.4b) has a global minimum in f_n at $n_* = 130$, which corresponds to a length of 5 rings. The additional local minima correspond to structures with 4, 6, and 7 closed rings respectively. Structures consisting entirely of closed rings are favored due to low edge energy. At larger sizes the free energy minimum structures exhibit cracks or correspond to multiple weakly-bound trumpets (each of which is self-limited). Note that structures corresponding to local minima in f_n with $n < n_*$ can be thermodynamically favored over the global minimum free energy structure at finite concentrations due to their greater translational entropy, whereas local minima with $n > n_*$

are not favored at any concentration (see Fig. 5 and Ref.[8]).

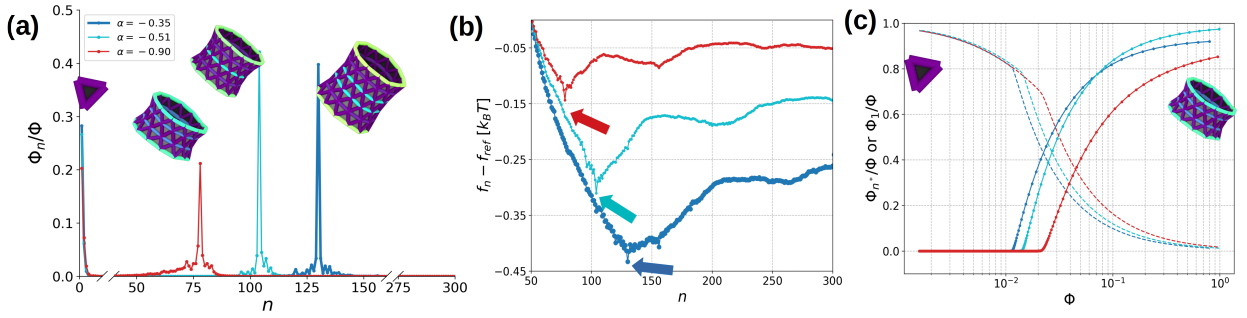

Figure 5: Equilibrium cluster size distributions in the canonical ensemble (NVT) computed from free energy profiles. **(a)** Distribution of subunits in n-clusters for $\beta = 0.5$ and three α values. To aid visibility, the total concentration Φ for each curve is set to make the peaks at the self-limited size and free subunits both visible: $\alpha = -0.35$ ($\Phi = 0.03$), $\alpha = -0.51$ ($\Phi = 0.04$), $\alpha = -0.9$ ($\Phi = 0.08$). **(b)** Per-subunit free energy profiles corresponding to the distributions in (a). Arrows indicate global minima (n_*). The profiles are shifted vertically by a reference value at $n = 50$. Note that the relatively small depth of the per-subunit global minima ($\approx 0.1 k_B T$) corresponds to a significant basin in the total grand free energy ($\sim n_*$). **(c)** Fraction of subunits that are free monomers or in clusters close to the optimal size, $n - n_* \in [-10, 10]$.

From the free energies f_n, we compute the cluster size distribution (fraction of subunits in clusters of size n, $\Phi_n = n \exp[-n(f_n - \mu_{\rm eq})]$) as a function of the total subunit density Φ, where the equilibrium chemical potential $\mu_{\rm eq}$ is determined by mass conservation $\Phi = \sum_n^{n_{\rm max}} \Phi_n$. We set the maximum structure size to $n_{\rm max} = 250$ because the umbrella sampling simulations sampled only up to $n = 300$; the results are not sensitive to $n_{\rm max}$ provided that $n_{\rm max} - n_*$ is sufficiently large that $\Phi_{n_{\rm max}} \to 0$. Fig. 5 shows the resulting cluster size distributions and corresponding free energy profiles for three systems with different self-limiting sizes $n^* = 78, 104, 130$, corresponding to a sequence of decreasing axial curvature anisotropies α. The increasing sizes of these minima are consistent with continuum theory expectations that the self-limiting trumpet lengths increase as axial curvature *decreases*, $L_* \sim \kappa_\parallel^{-2/5}$. In each case the distribution is sharply peaked with a maximum at a size that is approximately equal to the per-particle free energy minimum size n_* and is insensitive to the total concentration Φ. Analogous to classical aggregation, there is essentially no assembly below a pseudo-critical

total subunit concentration Φ_*; while for $\Phi \gg \Phi_*$ almost all subunits are in assemblies (with the monomer concentration approximately equal to Φ_*). In contrast to classical aggregation but analogous to curvature-controlled self-limited assembly of spherical micelles or capsids,[8] the assembly size distribution remains narrowly distributed around the optimal size n_*. We note that our simulation results do not strictly apply for $\Phi \gtrsim 0.1$ since the assumption of dilute noninteracting clusters breaks down; however, this occurs well above the CAC. Moreover, the CAC can be arbitrarily lowered by increasing binding affinities.

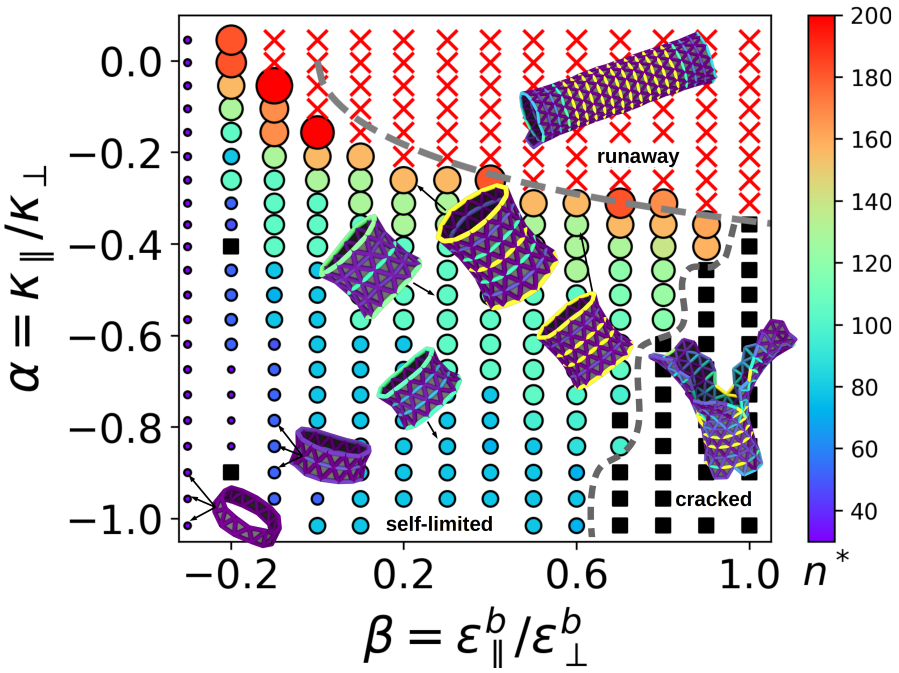

Figure 6: Equilibrium phase diagram in the $\alpha - \beta$ plane computed from umbrella sampling. Symbols indicate phases: self-limited (○), cracked (■), and runaway (×). For the self-limited phase, symbols are colored and sized according to the optimal size n_*. Parameter sets are categorized as *cracked* if the coefficient of variation of the open boundary length is larger than 0.5 at the lowest value of f_n; *self-limited* if they are not cracked and exhibit a global minimum at f_{n_*} with $n_* \leq 250$; and *runaway* if they are neither cracked nor exhibit a global minimum for $n \leq 250$. Phase boundaries are qualitatively insensitive to these criteria. The cracked-runaway phase boundary is drawn as a guide to the eye, while the runaway-self limited phase boundary is estimated from the scaling argument as $\alpha = -s[\beta/(\beta+2)]^{1/2}$, with the value of the unknown prefactor $s = 0.6$ set by eye. The $\alpha = 0$ and $\alpha = -1$ lines respectively correspond to preferred cylinder and minimal surface geometries, and $\beta = 1$ represents isotropic binding strength.

Having established the existence of self-limiting equilibrium assembly at finite tempera-

ture and concentrations, we now consider the parameters that determine this range and the self-limited size. Fig. 6 shows the phase behavior and (in the self-limited regime) optimal size n_* computed from umbrella sampling, as a function of the dimensionless parameters controlling the frustration (negative curvature, α) and binding anisotropy (β). We see that, notwithstanding the effects of thermal fluctuations and escape to low-symmetry morphologies, equilibrium self-limitation exists over a broad range of model parameters, with n_* increasing as $\alpha \to 0$, that is, as the negative curvature decreases and the preferred geometry approaches the unfrustrated cylinder. However, the curvature of the free energy profile near the minimum ($d^2 f_n/dn^2|_{n_*}$) tends to decrease with n_* (see, for example, Fig. 5 b), until the minimum disappears and the system enters the runaway phase. The shape of the self-limited/runaway phase boundary can be estimated using the continuum scaling arguments presented above and setting $L_* \sim L_{\rm flat}$. Using the simplest estimate for the line tension, $\Lambda = -\epsilon_{\|}^{\rm b} = 3\beta/(\beta+2)\langle\epsilon_{\rm b}\rangle$, gives that in the $\alpha - \beta$ plane $\alpha = -s[\beta/(\beta+2)]^{1/2}$ with s an unknown constant. Fig. 6 shows that, by setting the proportionality factor to a physically reasonable value $s = 0.6$, the predicted phase boundary qualitatively describes the separatrix between the runaway and self-limited phases for $\beta > 0$.

We also find that anisotropic binding, with lateral interactions stronger than inter-ring interactions ($\beta < 1$), is essential for stable self-limited structures for all parameter ranges we have simulated. As $\beta \to 1$, the structure is sufficiently stabilized by strong inter-ring interactions that it becomes energetically favorable to break lateral interactions (i.e. form cracks) to relax the negative-curvature frustration. Additionally, sufficiently strong inter-ring bonds overwhelm the flattening cost of axial unbending, and thus the threshold α value for runaway trumpets decreases with increasing β. Hence, in a regime of $\beta \lesssim 1$, we observe that the self-limiting assembly is cut-off at the *upper* size range (low $|\alpha|$) by the elastic shape flattening mechanism, and at the *lower* size range (high $|\alpha|$) by the *inelastic* mechanism of longitudinal cracking. As $\beta \to 1$, assembly transitions directly from cracked to runaway structures, without an intervening self-limiting regime. In principle the location of boundary

between the cracked and self-limited phases could be determined from the binding energy costs and corresponding elastic energy release associated with crack formation. However, due to the long-range nature strain fields in the frustrated regime, nucleation of a crack results in complex non-axisymmetric strains and particle displacements far across the structure that complicate a simplified analytical estimation.

Conclusions

In conclusion, we demonstrated that geometric frustration leads to equilibrium self-limitation over a finite, but specific, range of shape-misfit and binding anistropy, when accounting for entropic effects at finite temperatures and complex, inelastic frustration escape mechanisms possible in a discrete particle model. Importantly, the two dimensionless parameters that we focused on, targeted negative curvature and binding anisotropy, are experimentally controllable (e.g. with DNA origami[19,20,50] or polymer hydrogel particles[51,52]). Moreover, our results identify a design principle: self-limitation requires stronger circumferential binding than axial binding. In a separate work we will consider a detailed comparison between predictions of ground-state continuum thermodynamics and the finite-T assembly of our discrete subunit model to assess the range and utility of analytical theories for guiding the design and engineering of GF assembly. Finally, equilibrium self-limitation does not necessarily describe finite-time assembly; e.g. long-lived metastable intermediates (kinetic traps) may arise for far out-of-equilibrium initial states.[62,63] Thus, systematic dynamical simulations are needed to identify the self-limited regime under finite-time constraints.

Beyond the specific application of geometrically-programmed DNA origami particles, our study casts light on existing assemblies. Notably, one key model of the dynamical instability of microtubules is associated with a transition of protofilamentary units to adopt an outward, trumpet-like curvature. In the context of microtubules, the drive for outward curvature is assumed to be a non-equilibrium process, driven by hydrolysis of ATP bound to tubulin

dimers, which in turn destabilizes the lateral binding between protofilalments, facilitating their rapid depolymerization.[64–69] To our knowledge, the equilibrium implications, specifically the potential to stabilize of finite equilibrium lengths, of this geometric frustration has not yet been considered. More broadly, our model considers the frustration in elastic membranes that have a preference for negative Gaussian curvature. This general problem has been studied in the context of tape-like, helicoidal membranes,[41,42] which can have finite-dimensions in one of the two dimensions of the sheet, but grow to unlimited length. Notably, we show here that by directing one of the two directions to close upon itself, frustration can stabilize assemblies of finite *mass*, as opposed to finite spatial dimensions.

Methods

The model is adapted from the discrete subunit model previously developed for icosahedral shell self-assembly.[57–61] Here only edges with the same type can bind to each other, with binding energies $\epsilon_{\mathrm{b}}^{t}$ for edge-type $t = 1, 2, 3$. Two of the binding energies, corresponding to bonds within circumferential hoops, are equal, $\epsilon_{\mathrm{b}}^{1} = \epsilon_{\mathrm{b}}^{2} \equiv \epsilon_{\perp}^{\mathrm{b}}$, while the third is different, $\epsilon_{\mathrm{b}}^{3} = \epsilon_{\parallel}^{\mathrm{b}}$, corresponding to axial bonding. The in-plane stretching elasticity of the sheet derives from a Hookean energy penalty for deviations of each edge from its preferred length l_0, $E_{\mathrm{s}} = \epsilon_{\mathrm{s}}(l - l_0)^2/2$ with ϵ_{s} the edge's elastic modulus, and l its instantaneous length. Here, we set ϵ_{s} the same for all three edge types. The preferred curvatures and bending modulus are controlled by a bending potential on dihedral angles along bonds, $E_{\mathrm{bend}} = \kappa_{\mathrm{b}}\big(\theta^{m} - \theta_0^{t(m)}\big)^2/2$, with m the index of a bound edge pair and $\theta_0^{t(m)}$ the preferred dihedral angle across bonds between bound edge pairs of type $t(m)$ (Fig. 2b). Analogous to the binding energy, we set $\theta_0^1 = \theta_0^2 \equiv \theta_0^{\perp}$ and $\theta_0^3 \equiv \theta_0^{\parallel}$, which respectively set the preferred principal curvatures $\kappa_{\perp}$ and $\kappa_{\parallel}$. In the limit of small preferred curvatures, the trumpet assemblies can be approximated as frustrated elastic shells, with target principal curvatures $\kappa_{\perp} \approx \theta_0^{\perp}/\sqrt{3}$ and $\kappa_{\parallel} \approx (2\theta_0^{\parallel} + \theta_0^{\perp})/\sqrt{3}$ (see SI).

We perform simulations using a grand canonical (μVT) Monte Carlo (MC) algorithm. To model the limit of dilute, noninteracting assemblies (the most experimentally relevant regime) and to avoid kinetic traps associated with depletion of free subunits,[62] we simulate a single assembling structure in exchange with free subunits at fixed chemical potential μ. We compute the equilibrium grand potential Ω_n as a function of cluster size n, using umbrella sampling combined with parallel tempering to efficiently sample the rugged free energy landscape. The intra-cluster interaction free energy F_n is then obtained by subtracting the ideal subunit translational free energy, $F_n = \Omega_n + \mu n$.[8,40,70–73] Technical details are in the SI. The MC algorithm includes 11 moves (details are in the SI and ref.[74]) that account for subunit association/dissociation and structural relaxation of intermediates. We focus here on *equilibrium* self-limited states, for which the relative rates for different moves are irrelevant. However, the dynamics are not qualitatively sensitive to changing relative values of the rates (see SI Fig. 9).

The model parameters are the stretching modulus $\epsilon_{\rm s}$, the bending modulus $\kappa_{\rm b}$, the binding energies $\epsilon_{\perp}^{\rm b}$ and $\epsilon_{\parallel}^{\rm b}$,the preferred curvatures $\kappa_{\perp}$ and $\kappa_{\parallel}$, the chemical potential μ, and the MC move attempt rates. Due to the large parameter space, here we set the subunit elastic properties to $\epsilon_{\rm s} = 150 k_{\rm B}T/l_0^2$ and $\kappa_{\rm b} = 300 k_{\rm B}T$, and the standard state volume to $v_0 = l_0^3$. In addition, we fixed the average binding energy to $\langle \epsilon_{\rm b} \rangle = (2\epsilon_{\perp}^{\rm b} + \epsilon_{\parallel}^{\rm b})/3 = -6.5 k_{\rm B}T$ and the positive curvature $\kappa_{\perp} \approx 2\pi/(N_{\rm p} l_0)$ so that $2N_{\rm p} = 26$ subunits pack in an unstrained ring. Throughout the paper, we vary two dimensionless parameters: i) the curvature anisotropy: $\alpha = \kappa_{\parallel}/\kappa_{\perp}$ and ii) binding anisotropy $\beta = \epsilon_{\parallel}^{\rm b}/\epsilon_{\perp}^{\rm b}$.

Supporting Information. The suporting information available online contains details on the model and the Monte Carlo algorithm used to obtain the results presented above. We also present details on the free energy calculations using umbrella sampling combined with parallel tempering. Finally, we show how the preferred curvatures $\kappa_{\parallel}$ and $\kappa_{\perp}$ map to the preferred dihedral angles $\theta_0^{\parallel}$ and $\theta_0^{\perp}$. In addition to these details, we provide videos of the 3 trajectories corresponding to the self-limited, cracked and runaway phases of Fig. 4

and a video showing the structure evolution under cycling conditions to test the equilibrium sampling.

Acknowledgments

This work was supported by Award Number R01GM108021 from the National Institute Of General Medical Sciences (BT, FM, MFH), the Brandeis Center for Bioinspired Soft Materials, an NSF MRSEC, DMR-2011846 (BT, FM, DMH, GMH, MFH), and through NSF grant No. DMR-2028885 (DMH, GMG). Computational resources were provided by NSF XSEDE computing resources (grant No. TG-MCB090163, Stampede, Comet, Expanse) and the Brandeis HPCC which is partially supported by NSF DMR-2011846 and NSF OAC-1920147.

References

1. Zlotnick, A.; Mukhopadhyay, S. Virus assembly, allostery and antivirals. *Trends in Microbiology* **2011**, *19*, 14–23.

2. Mateu, M. G. Assembly, stability and dynamics of virus capsids. *Archives of Biochemistry and Biophysics* **2013**, *531*, 65–79.

3. Bruinsma, R. F.; Klug, W. S. Physics of viral shells. *Annual Review of Condensed Matter Physics* **2015**, *6*, 245–268.

4. Perlmutter, J. D.; Hagan, M. F. Mechanisms of virus assembly. *Annual Review of Physical Chemistry* **2015**, *66*, 217–239.

5. Hagan, M. F.; Zandi, R. Recent advances in coarse-grained modeling of virus assembly. *Current Opinion in Virology* **2016**, *18*, 36–43.

6. Twarock, R.; Bingham, R. J.; Dykeman, E. C.; Stockley, P. G. A modelling paradigm for RNA virus assembly. *Current Opinion in Virology* **2018**, *31*, 74–81.

7. Zandi, R.; Dragnea, B.; Travesset, A.; Podgornik, R. On virus growth and form. *Physics Reports* **2020**, *847*, 1–102.

8. Hagan, M. F.; Grason, G. M. Equilibrium mechanisms of self-limiting assembly. *Reviews of Modern Physics* **2021**, *93*, 25008.

9. Schmid, M. F.; Paredes, A. M.; Khant, H. A.; Soyer, F.; Aldrich, H. C.; Chiu, W.; Shively, J. M. Structure of Halothiobacillus neapolitanus Carboxysomes by Cryo-electron Tomography. *Journal of Molecular Biology* **2006**, *364*, 526–535.

10. Iancu, C. V.; Ding, H. J.; Morris, D. M.; Dias, D. P.; Gonzales, A. D.; Martino, A.; Jensen, G. J. The Structure of Isolated Synechococcus Strain WH8102 Carboxysomes as Revealed by Electron Cryotomography. *Journal of Molecular Biology* **2007**, *372*, 764–773.

11. Kerfeld, C. A.; Heinhorst, S.; Cannon, G. C. Bacterial microcompartments. *Annual Review of Microbiology* **2010**, *64*, 391–408.

12. Rae, B. D.; Long, B. M.; Badger, M. R.; Price, G. D. Functions, Compositions, and Evolution of the Two Types of Carboxysomes: Polyhedral Microcompartments That Facilitate CO 2 Fixation in Cyanobacteria and Some Proteobacteria . *Microbiology and Molecular Biology Reviews* **2013**, *77*, 357–379.

13. Chowdhury, C.; Sinha, S.; Chun, S.; Yeates, T. O.; Bobik, T. A. Diverse Bacterial Microcompartment Organelles. *Microbiology and Molecular Biology Reviews* **2014**, *78*, 438–468.

14. Kerfeld, C. A.; Melnicki, M. R. Assembly, function and evolution of cyanobacterial carboxysomes. *Current Opinion in Plant Biology* **2016**, *31*, 66–75.

15. Sutter, M.; Boehringer, D.; Gutmann, S.; Günther, S.; Prangishvili, D.; Loessner, M. J.; Stetter, K. O.; Weber-Ban, E.; Ban, N. Structural basis of enzyme encapsulation into a bacterial nanocompartment. *Nature Structural and Molecular Biology* **2008**, *15*, 939–947.

16. Pfeifer, F. Distribution, formation and regulation of gas vesicles. *Nature Reviews Microbiology* **2012**, *10*, 705–715.

17. Nott, T. J.; Petsalaki, E.; Farber, P.; Jervis, D.; Fussner, E.; Plochowietz, A.; Craggs, T. D.; Bazett-Jones, D. P.; Pawson, T.; Forman-Kay, J. D.; Baldwin, A. J. Phase Transition of a Disordered Nuage Protein Generates Environmentally Responsive Membraneless Organelles. *Molecular Cell* **2015**, *57*, 936–947.

18. Zaslavsky, B. Y.; Ferreira, L. A.; Darling, A. L.; Uversky, V. N. The solvent side of proteinaceous membrane-less organelles in light of aqueous two-phase systems. *International Journal of Biological Macromolecules* **2018**, *117*, 1224–1251.

19. Sigl, C.; Willner, E. M.; Engelen, W.; Kretzmann, J. A.; Sachenbacher, K.; Liedl, A.; Kolbe, F.; Wilsch, F.; Aghvami, S. A.; Protzer, U.; Hagan, M. F.; Fraden, S.; Dietz, H. Programmable icosahedral shell system for virus trapping. *Nature Materials* **2021**,

20. Wagenbauer, K. F.; Sigl, C.; Dietz, H. Gigadalton-scale shape-programmable DNA assemblies. *Nature* **2017**, *552*, 78–83.

21. Bale, J. B.; Gonen, S.; Liu, Y.; Sheffler, W.; Ellis, D.; Thomas, C.; Cascio, D.; Yeates, T. O.; Gonen, T.; King, N. P.; Baker, D. Accurate design of megadalton-scale two-component icosahedral protein complexes. *Science* **2016**, *353*, 389–394.

22. Divine, R.; Dang, H. V.; Ueda, G.; Fallas, J. A.; Vulovic, I.; Sheffler, W.; Saini, S.; Zhao, Y. T.; Raj, I. X.; Morawski, P. A.; Jennewein, M. F.; Homad, L. J.; Wan, Y. H.; Tooley, M. R.; Seeger, F.; Etemadi, A.; Fahning, M. L.; Lazarovits, J.; Roederer, A.;

Walls, A. C. *et al.* Designed proteins assemble antibodies into modular nanocages. *Science* **2021**, *372*.

23. Butterfield, G. L.; Lajoie, M. J.; Gustafson, H. H.; Sellers, D. L.; Nattermann, U.; Ellis, D.; Bale, J. B.; Ke, S.; Lenz, G. H.; Yehdego, A.; Ravichandran, R.; Pun, S. H.; King, N. P.; Baker, D. Evolution of a designed protein assembly encapsulating its own RNA genome. *Nature* **2017**, *552*, 415–420.

24. King, N. P.; Bale, J. B.; Sheffler, W.; McNamara, D. E.; Gonen, S.; Gonen, T.; Yeates, T. O.; Baker, D. Accurate design of co-assembling multi-component protein nanomaterials. *Nature* **2014**, *510*, 103–108.

25. Lai, Y. T.; Reading, E.; Hura, G. L.; Tsai, K. L.; Laganowsky, A.; Asturias, F. J.; Tainer, J. A.; Robinson, C. V.; Yeates, T. O. Structure of a designed protein cage that self-assembles into a highly porous cube. *Nature Chemistry* **2014**, *6*, 1065–1071.

26. Levasseur, M. D.; Mantri, S.; Hayashi, T.; Reichenbach, M.; Hehn, S.; Waeckerle-Men, Y.; Johansen, P.; Hilvert, D. Cell-Specific Delivery Using an Engineered Protein Nanocage. *ACS Chem. Biol.* **2021**, *16*, 838–843.

27. Noble, J. E.; De Santis, E.; Ravi, J.; Lamarre, B.; Castelletto, V.; Mantell, J.; Ray, S.; Ryadnov, M. G. A De Novo Virus-Like Topology for Synthetic Virions. *J. Am. Chem. Soc.* **2016**, *138*, 12202–12210.

28. Edwardson, T.; Mori, T.; Hilvert, D. Rational Engineering of a Designed Protein Cage for siRNA Delivery. *J. Am. Chem. Soc.* **2018**, *140*, 10439–10442.

29. Mosayebi, M.; Shoemark, D. K.; Fletcher, J. M.; Sessions, R. B.; Linden, N.; Woolfson, D. N.; Liverpool, T. B. Beyond icosahedral symmetry in packings of proteins in spherical shells. *Proceedings of the National Academy of Sciences* **2017**, *114*, 9014–9019.

30. Makowski, L.; Magdoff-Fairchild, B. Polymorphism of sickle cell hemoglobin aggregates: structural basis for limited radial growth. *Science* **1986**, *234*, 1228–1231.

31. Weisel, J. W. The mechanical properties of fibrin for basic scientists and clinicians. *Biophysical Chemistry* **2004**, *112*, 267–276.

32. Grason, G. M. Perspective: Geometrically frustrated assemblies. *Journal of Chemical Physics* **2016**, *145*, 1–17.

33. Lenz, M.; Witten, T. A. Geometrical frustration yields fibre formation in self-assembly. *Nature Physics* **2017**, *13*, 1100–1104.

34. Meiri, S.; Efrati, E. Cumulative geometric frustration in physical assemblies. 2021; `http://arxiv.org/abs/2101.09816`, acessed May 20, 2022.

35. Hall, D. M.; Bruss, I. R.; Barone, J. R.; Grason, G. M. Morphology selection via geometric frustration in chiral filament bundles. *Nature Materials* **2016**, *15*, 727–732.

36. Weisel, J. W.; Nagaswami, C.; Makowski, L. Twisting of fibrin fibers limits their radial growth. *Proceedings of the National Academy of Sciences of the United States of America* **1987**, *84*, 8991–8995.

37. Bruss, I. R.; Grason, G. M. Topological defects, surface geometry and cohesive energy of twisted filament bundles. *Soft Matter* **2013**, *9*, 8327–8345.

38. Haddad, A.; Aharoni, H.; Sharon, E.; Shtukenberg, A. G.; Kahr, B.; Efrati, E. Twist renormalization in molecular crystals driven by geometric frustration. *Soft Matter* **2019**, *15*, 116–126.

39. Turner, M. S.; Briehl, R. W.; Ferrone, F. A.; Josephs, R. Twisted Protein Aggregates and Disease: The Stability of Sickle Hemoglobin Fibers. *Physical Review Letters* **2003**, *90*, 4.

40. Yang, Y.; Meyer, R. B.; Hagan, M. F. Self-limited self-assembly of chiral filaments. *Physical Review Letters* **2010**, *104*, 1–4.

41. Armon, S.; Aharoni, H.; Moshe, M.; Sharon, E. Shape selection in chiral ribbons: From seed pods to supramolecular assemblies. *Soft Matter* **2014**, *10*, 2733–2740.

42. Ghafouri, R.; Bruinsma, R. Helicoid to spiral ribbon transition. *Physical Review Letters* **2005**, *94*, 1–4.

43. Schneider, S.; Gompper, G. Shapes of crystalline domains on spherical fluid vesicles. *Europhysics Letters* **2005**, *70*, 136–142.

44. Chen, Z.; Huang, G.; Trase, I.; Han, X.; Mei, Y. Mechanical Self-Assembly of a Strain-Engineered Flexible Layer: Wrinkling, Rolling, and Twisting. *Physical Review Applied* **2016**, *5*, 1–33.

45. Guo, Q.; Mehta, A. K.; Grover, M. A.; Chen, W.; Lynn, D. G.; Chen, Z. Shape selection and multi-stability in helical ribbons. *Applied Physics Letters* **2014**, *104*.

46. Efrati, E. Non-Euclidean Ribbons: Generalized Sadowsky Functional for Residually-Stressed Thin and Narrow Bodies. *Journal of Elasticity* **2015**, *119*, 251–261.

47. Francesco, S.; Lu, J.; Kotov, N.; Kai, S.; Xiaoming, M. Frustrated self-assembly of non-Euclidean crystals of nanoparticles. *Nature Communications* **2021**, *12*, 1–17.

48. Hall, D. M.; Grason, G. M. How geometric frustration shapes twisted fibres, inside and out: Competing morphologies of chiral filament assembly. *Interface Focus* **2017**, *7*.

49. Gelbart, A. B.-S., W.; Roux, D. In *Micelles, Membranes, Microemulsions and Monolayers*; Springer, New York,, Ed.; 1994.

50. Bollinger, J. A.; Stevens, M. J. Diverse balances of tubulin interactions and shape change drive and interrupt microtubule depolymerization. *Soft Matter* **2019**, *15*, 8137–8146.

51. Bae, J.; Na, J. H.; Santangelo, C. D.; Hayward, R. C. Edge-defined metric buckling of temperature-responsive hydrogel ribbons and rings. *Polymer* **2014**, *55*, 5908–5914.

52. Kim, J.; Hanna, J. A.; Hayward, R. C.; Santangelo, C. D. Thermally responsive rolling of thin gel strips with discrete variations in swelling. *Soft Matter* **2012**, *8*, 2375–2381.

53. Hayakawa, D.; Videbæk, T. E.; Hall, D. M.; Fang, H.; Sigl, C.; Feigl, E.; Dietz, H.; Fraden, S.; Hagan, M. F.; Grason, G. M.; Rogers, W. B. Geometrically programmed self-limited assembly of tubules using DNA origami colloids. 2022; `http://arxiv.org/abs/2203.01421`, accessed May 20, 2022.

54. Stevens, M. J. The long persistence length of model tubules. *Journal of Chemical Physics* **2017**, *147*.

55. Seung, H. S.; Nelson, D. R. Defects in flexible membranes with crystalline order. *Physical Review A* **1988**, *38*, 1005–1018.

56. Stukowski, A. Visualization and analysis of atomistic simulation data with OVITO-the Open Visualization Tool. *Modelling and Simulation in Materials Science and Engineering* **2010**, *18*.

57. Rotskoff, G. M.; Geissler, P. L. Robust nonequilibrium pathways to microcompartment assembly. *Proceedings of the National Academy of Sciences of the United States of America* **2018**, *115*, 6341–6346.

58. Li, S.; Roy, P.; Travesset, A.; Zandi, R. Why large icosahedral viruses need scaffolding proteins. *Proceedings of the National Academy of Sciences of the United States of America* **2018**, *115*, 10971–10976.

59. Wagner, J.; Zandi, R. The Robust Assembly of Small Symmetric Nanoshells. *Biophysical Journal* **2015**, *109*, 956–965.

60. Panahandeh, S.; Li, S.; Marichal, L.; Leite Rubim, R.; Tresset, G.; Zandi, R. How a Virus Circumvents Energy Barriers to Form Symmetric Shells. *ACS Nano* **2020**, *14*, 3170–3180.

61. Panahandeh, S.; Li, S.; Zandi, R. The equilibrium structure of self-assembled protein nano-cages. *Nanoscale* **2018**, *10*, 22802–22809.

62. Hagan, M. F. Modeling Viral Capsid Assembly. *Adv. Chem. Phys.* **2014**, *155*, 1–68.

63. Whitelam, S.; Jack, R. L. The statistical mechanics of dynamic pathways to self-assembly. *Annual Review of Physical Chemistry* **2015**, *66*, 143–163.

64. Alushin, G. M.; Lander, G. C.; Kellogg, E. H.; Zhang, R.; Baker, D.; Nogales, E. High-resolution microtubule structures reveal the structural transitions in alphabeta-tubulin upon GTP hydrolysis. *Cell* **2014**, *157*, 1117–29.

65. Hemmat, M.; Odde, D. J. Atomistic basis of microtubule dynamic instability assessed via multiscale modeling. 2020; `https://www.biorxiv.org/content/early/2020/01/08/2020.01.07.897439`, accessed May 20, 2022.

66. Michaels, T. C.; Feng, S.; Liang, H.; Mahadevan, L. Mechanics and kinetics of dynamic instability. *Elife* **2020**, *9*.

67. Tong, D.; Voth, G. A. Microtubule Simulations Provide Insight into the Molecular Mechanism Underlying Dynamic Instability. *Biophysical Journal* **2020**, *118*, 2938–2951.

68. VanBuren, V.; Cassimeris, L.; Odde, D. J. Mechanochemical Model of Microtubule Structure and Self-Assembly Kinetics. *Biophysical Journal* **2005**, *89*, 2911–2926.

69. Vulevic, B.; Correia, J. J. Thermodynamic and structural analysis of microtubule assembly: the role of GTP hydrolysis. *Biophysical Journal* **1997**, *72*, 1357–1375.

70. Frenkel, D.; Smit, B. In *Understanding molecular simulation: From algorithms to applications*; Academic Press, San Diego,, Ed.; 2002.

71. Earl, D. J.; Deem, M. W. Parallel tempering: Theory, applications, and new perspectives. *Physical Chemistry Chemical Physics* **2005**, *7*, 3910–3916.

72. Ferguson, A. L. BayesWHAM: A Bayesian approach for free energy estimation, reweighting, and uncertainty quantification in the weighted histogram analysis method. *Journal of Computational Chemistry* **2017**, *38*, 1583–1605.

73. Kumar, S.; Bouzida, D.; Swendsen, R. H.; Kollman, P. A.; Rosenberg, J. M. The weighted histogram analysis method for free-energy calculations on biomolecules. *Journal of computational chemistry* **1992**, *13*, 1011–1021.

74. Botsch, M.; Steinberg, S.; Bischoff, S.; Kobbelt, L. OpenMesh – a generic and efficient polygon mesh data structure. OpenSG Symposium. 2002.

Thermodynamic size control in curvature-frustrated tubules: Self-limitation with open boundaries Supplementary information

Botond Tyukodi,[1] Farzaneh Mohajerani,[1] Douglas M. Hall,[2] Gregory M. Grason,[2] and Michael F. Hagan[1]

[1] *Brandeis University, Waltham, USA*
[2] *UMass Amherst, Amherst, USA*

(Dated: September 6, 2021)

I. THE MODEL

In this section we provide additional details about the model and Monte Carlo simulation that we used to generate the results in the main text. The model and algorithm are similar to the one used to describe microcompartment assembly in ref. [1] by Rotskoff and Geissler (which we refer to as the RG model henceforth). In particular, we consider flexible triangular subunits which can bind to each other along edges with a set of preferred dihedral angles that set the preferred curvatures of the assembling sheet. Monte Carlo simulations are performed in the grand canonical ensemble at fixed μVT, with μ the chemical potential of subunits in the bath. Each Monte Carlo simulation involves a single cluster undergoing assembly and disassembly, with subunits taken from or returned to the bath respectively, as well as structural relaxation moves. We describe specific differences with respect to the RG model below.

1. Energies

In the trumpet model, each three edges of the triangular subunits are of different types, $t(p) = 1, 2, 3$, for edge index p and each edge can only bind to an edge of the same type on a neighboring subunit.

The total energy of the system is given by

$$E = \sum_{p}^{3n_{\mathrm{s}}} E^{p}_{\mathrm{stretch}} + \frac{1}{2}\sum_{\langle pq\rangle} (E^{pq}_{\mathrm{bend}} + E^{pq}_{\mathrm{bind}}) \tag{1}$$

where the first sum goes over all edges, with n_{s} the number of subunits in the cluster. The second sum only goes over bound edges (i.e. non-boundary, adjacent edges, so there are $2n_{\mathrm{b}}$ terms in the sum, with n_{b} as the number of bonds). The 1/2 factor corrects for double counting.

The stretching energy is defined as:

$$E^{p}_{\mathrm{stretch}} = \epsilon_{\mathrm{s}} \frac{(l^{p} - l_0)^2}{2} \tag{2}$$

where ϵ_{s} is the stretching modulus, l^p is the instantaneous length, and l_0 is the stress-free (rest) length of an edge. For the trumpet model we set the stretching modulus and rest length equal for all edges.

The bending energy is quadratic in deviations from the preferred dihedral angle:

$$E^{pq}_{\mathrm{bend}} = \kappa_{\mathrm{b}} \frac{\left(\theta^{pq} - \theta_0^{t(p)t(q)}\right)^2}{2} \tag{3}$$

with p and q adjacent edges and $t(p), t(q)$ the edge types. κ_{b} is the bending modulus and is set equal for all edge types. $\theta_0^{t(p)t(q)}$ is the preferred dihedral angle between edges with types $t(p)$ and $t(q)$. Since only edges of the same types are allowed to bind to each other, $t(p) = t(q) \equiv t$ for all adjacent edge pairs pq, and $\theta_0^{t(p)t(q)} \equiv \theta_0^t$. Two of the types are set to have the same, positive preferred dihedral $\theta_0^1 = \theta_0^2 \equiv \theta_0^{\perp}$ and the third one is set to have a different, negative preferred dihedral $\theta_0^3 \equiv \theta_0^{\parallel}$.

The binding energy between two edges p and q (with the same type $t(p) = t(q) = t$) is given by

$$E^{t}_{\mathrm{bind}} = \epsilon^{t}_{\mathrm{b}} \tag{4}$$

Similar to the preferred dihedrals, the two binding energies corresponding to the $\theta_0^{\perp}$ edges are set equal to $\epsilon_{\mathrm{b}}^1 = \epsilon_{\mathrm{b}}^2 \equiv \epsilon_{\perp}^{\mathrm{b}}$ and the third is set different, to $\epsilon_{\mathrm{b}}^3 = \epsilon_{\parallel}^{\mathrm{b}}$. A stronger (i.e. more negative) $\epsilon_{\perp}^{\mathrm{b}}$ favors intra-ring binding whereas $\epsilon_{\parallel}^{\mathrm{b}}$ is responsible for inter-ring binding.

In addition to the above terms, each subunit has at its center of mass a spherical excluder of radius $0.2l_0$ to prevent subunit overlaps. Finally, to prevent extreme distortions of subunits, maximum edge length fluctuations are limited to $l_0/2 < l < 3l_0/2$.

2. Coarse-graining

Our model is motivated by the triangular DNA origami subunits developed in Sigl et al.[2], in which subunits bind through lock-and-key 'patches' along subunit edges in which attractive interactions are generated through blunt-end

stacking of unsatisfied nucleotides. Therefore, in our model we define attractive bonds along subunit edges (rather than at vertices as in the RG model). In particular, attractive bonds occur at each shared pair of subunit edges with the same type. Because the interactions in the experimental system are driven by nucleotide stacking, they are extremely short-ranged in comparison to the subunit size (the subunit edge lengths are approximately 60 nm). Therefore, in our simulations we avoid resolving the short length scale fluctuations in separation distance between bound edges and their associated vertices by coarse-graining as follows.

A microstate i is defined as the position of all the $3n_{\rm s}$ vertices of $n_{\rm s}$ subunits: $i \rightarrow (\vec{x}_1, \vec{x}_2, ...\vec{x}_{3n_{\rm s}})$ The grand canonical probability *density* of finding the system around state i is

$$f(i) = \frac{P(\vec{x}_1, \vec{x}_1 + d\vec{x}_1; ...; \vec{x}_1, \vec{x}_{n_s} + d\vec{x}_{n_s})}{d\vec{x}_1 d\vec{x}_2 ... d\vec{x}_{3n_{\rm s}}} = \frac{1}{Z_\Omega} \frac{e^{\beta n_{\rm s} \mu}}{\lambda^{9n_{\rm s}}} e^{-\beta E_i} \tag{5}$$

where μ is the chemical potential and λ^3 is the standard state volume. This probability density has the dimensions of $1/\text{volume}^{3n_{\rm s}}$ corresponding to all the $3n_{\rm s}$ vertices of the subunits. Due to bonds, however, some pairs of vertices are confined within a *binding volume* $v_{\rm a}$. We consider a square-well potential so that the binding energy is constant within this volume. Analogous to Ref. [1], we can then coarse-grain to avoid resolving intra-bond fluctuations. We assume that fluctuations of bound edges are sufficiently small that each pair of vertices at either end of a bound edge pair are constrained within a *binding volume* $v_{\rm a}$. Note that we constrain vertices rather than edges so that the coarse-grained microstate can be represented in terms of positions of vertices rather than edges, which is easier to implement computationally. In the coarse-grained system, a coarse microstate is specified by the coordinates corresponding to the independent vertex degrees of freedom (with 1 degree of freedom for each bound vertex group and unbound vertex): $\Gamma \rightarrow (\vec{x}_1, \vec{x}_2, ...\vec{x}_{n_{\rm v}})$, where $n_{\rm v}$ is the number of independent bound vertex groups and free vertices. The probability of such a coarse-grained state is given by the net weight of all the corresponding fine-grained microstates:

$$\rho(\Gamma) = \int_{\{v_{\rm a}\}} f(i) {\rm d}^{n_{\rm VB}} \vec{x} \tag{6}$$

where $n_{\rm VB}$ is the number of vertex-bonds and is given by $n_{\rm VB} = 3n_{\rm s} - n_{\rm v}$. For simplicity, we take the limit in which $\sqrt[3]{v_{\rm a}}$ is small in comparison to the length scale over which the elastic energy varies, so that the energy is constant within the bound volume $v_{\rm a}$. Then $f(i)$ is a constant, and the probability density is given by

$$\rho(\Gamma) = \frac{1}{Z_\Omega} v_{\rm a}^{n_{\rm VB}} \frac{e^{\beta n_{\rm s} \mu}}{\lambda^{9n_{\rm s}}} e^{-\beta E_\Gamma} \tag{7}$$

where E_Γ is the total energy of state Γ (including stretching, bending and binding energies). The coarse graining process is illustrated in Fig. 1.

Differences from the RG model [1]. First, in our model attractive bonds are defined along shared edges, while attractive bonds are counted at grouped vertices in the RG model. Thus, in our model the number of bonds $n_{\rm b}$ for a given configuration is equal to the number of shared edges, whereas in the RG model it would be equal to the number vertex bonds, $n_{\rm VB}$. However, the Hamiltonian for the elastic energy of the triangulated sheet and the corresponding Monte Carlo algorithm are much more straightforward to define in terms of a set of vertex positions rather than edge positions and orientations. Therefore, in our simulations we track vertex positions, by following the coarse-graining procedure described above. The distinction between attractions at edge- or vertex-pairs does not lead to qualitative differences between our model in the RG model, but it does imply that the binding affinity values $\epsilon_{\rm b}$ and the binding volume $v_{\rm a}$ must be treated as independent parameters in our model, since in general the number of bound vertices is not identical to the number of bound edges. Note that both definitions (bonds along edges or bonds at vertex pairs) involve approximations to the rotational and translational entropy penalties associated with subunit binding, since they assume a constant entropy penalty for each vertex degree of freedom that is lost within a bound vertex group, independent of the local environment (i.e., the number of bonds that a given subunit has) [3, 4].

Second, because we are modeling independent triangular subunits binding along edges, each unbound edge in the graph (those edges at the boundary of the structure) correspond to a single physical subunit edge, while bound edges (those in the structure interior) each correspond to two physical subunit edges. Therefore, in our model we set the stretching modulus for a bound edge to be twice that of a free edge. In the RG model all edges have the same stretching modulus.

3. Implementation and data structure

The simulation is implemented on top of the OpenMesh library [5]. Subunits are implemented as triangular mesh elements. OpenMesh uses the halfedge data structure which is suitable to implement triangles with directed normals

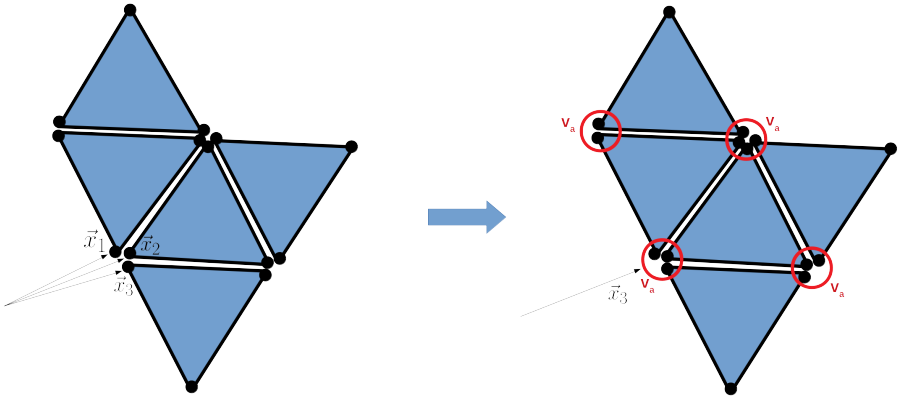

FIG. 1. Coarse-graining of an example cluster configuration. In this configuration, the number of subunits is $n_\mathrm{s} = 5$, the number of initial (before coarse-graining) vertices is $3n_\mathrm{s} = 15$, and the number of vertices after coarse-graining is $n_\mathrm{v} = 7$. The red circles indicate bound vertex groups, and the number of vertex degrees of freedom that have been eliminated by coarse-graining in this configuration is $n_\mathrm{VB} = 1 + 3 + 2 + 2 = 8 = 3n_\mathrm{s} - n_\mathrm{v}$. Motivated by DNA origami subunits in Sigl et al. [2], the attractive interactions (i.e. 'bonds') in this model occur along edge-pairs of the same type shared by two subunits. In this configuration there are $n_\mathrm{b} = 4$ bonds.

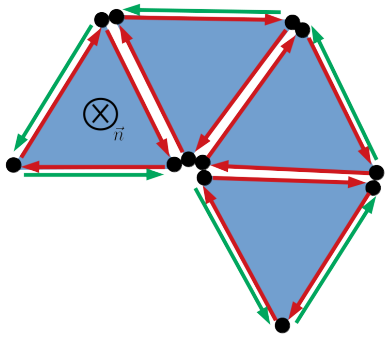

FIG. 2. The halfedge data structure used by OpenMesh. Each edge is represented by two directed edges. Boundary edges are no exception and thus are represented by a non-boundary halfedge and a boundary halfedge (in green). This latter is irrelevant for our model. Directed edges allow for the unambiguous definition of face normals, for efficient iterations of the element's neighborhood as well as boundary iterations.

(Fig 2). The directed halfedges allow for a clockwise iteration through the boundary of a triangle, which makes the two faces of the triangles distinguishable. Only halfedges with opposite orientations can bind together, making it impossible to form a Mobius strip, for example. The data structure and the resulting iterators in OpenMesh allow for an easy and efficient iteration over the neighborhood of mesh elements (vertices, edges and faces). The implementation of mesh element rearrangements is less straightforward, but we implemented it via the insertion and removal of virtual triangles. In addition, OpenMesh allows for the storage of various properties on mesh elements, allowing storage of edge types and face types stored on the elements. To improve readability in the upcoming sections, we will not represent halfedges separately.

II. THE MONTE CARLO MOVES

In this section we detail the Monte Carlo moves of the simulation. Our algorithm has 11 moves: vertex displacement, simple subunit insertion/deletion, wedge insertion/deletion, wedge fusion/fission, crack fusion/fission, and edge fusion/fission.

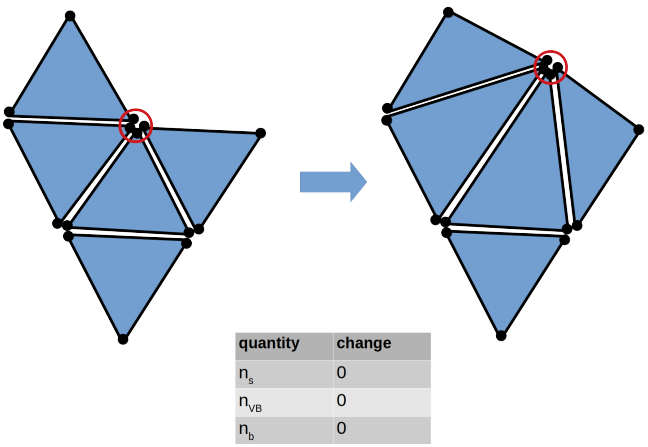

quantity	change
n_s	0
n_{VB}	0
n_b	0

FIG. 3. Vertex move. A vertex is randomly displaced and the move is accepted according to the usual Metropolis probability.

Detailed balance. For the transition between state Γ and Γ' detailed balance corresponds to [1, 6]:

$$P(\Gamma) \times \alpha(\Gamma \to \Gamma') \times p_{\rm acc}(\Gamma \to \Gamma') = P(\Gamma') \times \alpha(\Gamma' \to \Gamma) \times p_{\rm acc}(\Gamma' \to \Gamma) \tag{8}$$

where $\alpha(\Gamma \to \Gamma')$ is the probability of generating a $\Gamma \to \Gamma'$ move attempt (trial), $p_{\rm acc}(\Gamma \to \Gamma')$ is the probability of accepting the move, and $P(\Gamma) = \rho(\Gamma) {\rm d}^{n_{\rm v}(\Gamma)}\vec{x}$ is the equilibrium probability of finding a system in a voxel of volume ${\rm d}^{n_{\rm v}(\Gamma)}\vec{x}$.

Next, we use Eq. (8) to define the acceptance criteria for each MC move. The acceptance criteria are derived in detail for the wedge fusion/fission move; the steps to follow are the same for all other moves.

A. Vertex displacement

In this move, a vertex is randomly selected, a random uniform displacement is drawn, and the vertex is displaced to its new position according to:

$$x \to x + \mathcal{U}(-d_{\rm max}, d_{\rm max}) \tag{9}$$
$$y \to y + \mathcal{U}(-d_{\rm max}, d_{\rm max}) \tag{10}$$
$$z \to z + \mathcal{U}(-d_{\rm max}, d_{\rm max}) \tag{11}$$

with $d_{\rm max}$ the maximum displacement. The move is accepted with a probability $p_{\rm acc} = \exp(-\Delta E/k_{\rm B}T)$ where ΔE is the (bending plus stretching) energy change due to the displacement. The parameter $d_{\rm max}$ can be adjusted during a burn-in period to optimize convergence to equilibrium. Generally optimal values are on the order of the typical length scale of thermal fluctuations dictated by the elastic energy, leading to acceptance probabilities on the order of 50%. In our simulations typical values are between $d_{\rm max} = [0.01l_0, 0.1l_0]$. The vertex displacement move is illustrated in Fig 3: the number of subunits $n_{\rm s}$, number of vertices $n_{\rm v}$, number of vertex bonds $n_{\rm VB}$ and number of bonds $n_{\rm b}$ remains unchanged during this move.

B. Simple insertion / removal

1. *Simple insertion*

In this move, an edge is randomly selected from the set of all boundary edges, where a new subunit will be attached. The number of such boundary edges is $n_{\rm e}$. Subunits can be inserted in $n_{\rm r}$ different rotations, where $n_{\rm r}$ is the number of distinct rotational states for a subunit which has one edge aligned with the edge of a neighboring subunit. For our triangular subunits with three distinct edge types, $n_{\rm r} = 3$. In our algorithm, during insertion of a subunit its rotational state is chosen randomly from the set of three possibilities. If the aligned edge is not complementary to

the type of the boundary edge, then the move is rejected. In this work, the two edges must be of the same type to be complementary.

The positions of two of the new subunit's vertices (those at either end of the edge being bound) are set equal to the positions of the corresponding vertices of the boundary edge to which it is binding. The third vertex position is randomly chosen from within a volume $v_{\rm add}$ centered at the equilibrium position of the new vertex.

Thus, the attempt probability for a simple insertion is given by:

$$\alpha(i \to j) = n_{\rm e} k_{\rm i} \tau n_{\rm r} \times \frac{1}{n_{\rm e} n_{\rm r} (v_{\rm add}/{\rm d}\vec{x})}. \tag{12}$$

Then, applying Eq. (8) and the attempt probability for the reverse move (simple deletion, presented next, Eq. (14)), the acceptance probabilities for a simple insertion is

$$p_{\rm acc}(i \to j) = \min\left[1, \frac{v_{\rm a}^2 v_{\rm add}}{\lambda^9} \exp[-(\Delta E_{i\to j} - \mu)/k_{\rm B}T]\right]. \tag{13}$$

$\Delta E_{i\to j}$ is the energy change due to the move and includes the stretching energy of the newly inserted subunit, its bending energy along the shared edge, and the binding energy due to the creation of an extra bond. During this move, one new (edge) bond and two new vertex bonds are created; i.e. $n_{\rm b} \to n_{\rm b} + 1$ and $n_{\rm VB} \to n_{\rm VB} + 2$. Moreover, the number of vertices in the structure increases by one, $n_{\rm v} \to n_{\rm v} + 1$.

2. Simple removal

The reverse move to simple insertion is simple removal. Subunits that can be deleted with this move are those with two boundary edges. The number of simply removable subunits is $n_{\rm sr}$. One of these is selected randomly, so the attempt probability is

$$\alpha(j \to i) = n_{\rm sr} k_{\rm i} \tau \times \frac{1}{n_{\rm sr}} \tag{14}$$

and, using Eq. (8) and Eq. (12), the acceptance probability is

$$p_{\rm acc}(j \to i) = \min\left[1, \frac{\lambda^9}{v_{\rm a}^2 v_{\rm add}} \exp[-(\Delta E_{j\to i} + \mu)/k_{\rm B}T]\right] \tag{15}$$

During this move, the structure loses one (edge) bond and two vertex bonds; $n_{\rm b} \to n_{\rm b} - 1$ and $n_{\rm VB} \to n_{\rm VB} - 2$. The number of vertices in the structure decreases by one, $n_{\rm v} \to n_{\rm v} - 1$.

If there are multiple species with chemical potentials μ_k, detailed balance must be satisfied for each species, individually. Moreover, each species can have different insertion rates $k_{\rm i}^k$.

To keep $\alpha < 1$, we ensure that the insertion rate $k_{\rm i}$ constrained by

$$n_{\rm e} k_{\rm i} \tau n_{\rm r} < 1 \tag{16}$$

$$n_{\rm sr} k_{\rm i} \tau < 1 \tag{17}$$

In equilibrium, one can use adaptive rates, i.e. reduce k_i on the run if the above condition is not satisfied. In that case, sampling is not taken for the ensuing several time steps. Alternatively, the rates may be set to a low enough value from the beginning and only tested on the run to ensure that the $\alpha < 1$ condition is satisfied. This latter technique is appropriate for dynamical runs as it keeps the rates constant throughout the simulation.

Moreover, we must ensure that $v_{\rm add}$ is large enough so that the vertex does not leave the $v_{\rm add}$ volume during structural relaxation moves; otherwise the insertion/deletion moves would not be reversible and the detailed balance would be violated. For a better convergence, one could choose a gaussian distribution $\mathcal{N}(\vec{r})$ for the position of the new vertex instead of a uniform distribution $1/v_{\rm add}$. In this case, this distribution has to be accounted for in the acceptance probabilities $p_{\rm acc}(i \to j)$ and $p_{\rm acc}(j \to i)$.

C. Wedge insertion/removal

1. Wedge insertion

Wedges are positions in the structure where a triangle can be inserted via attaching to two edges (Fig. 5). In a wedge move, we pick randomly from the set of available wedge positions in the structure, and pick a random orientation for

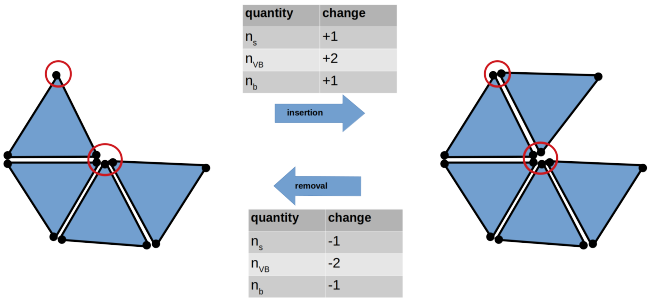

FIG. 4. Simple insertion and removal.

the new subunit. Denoting the number of wedge positions in a given structure as $n_{\rm w}$, the attempt probability for a wedge move is

$$\alpha(i \to j) = n_{\rm w} k_{\rm i} \tau n_{\rm r} \times \frac{1}{n_{\rm r} n_{\rm w}} \tag{18}$$

In contrast to the simple insertion move, there is no need for random vertex displacement in a wedge move because all three vertices of the new subunit are fixed by the three vertices of the wedge position. Combining Eq. (18) and the attempt probability for wedge removal (Eq. (20)), The acceptance probability for a wedge insertion is

$$p_{\rm acc}(i \to j) = \min\left[1, \frac{v_{\rm a}^3}{\lambda^9} \exp[-(\Delta E_{i\to j} - \mu)/k_{\rm B}T]\right]. \tag{19}$$

During a wedge insertion, two edge bonds and three vertex bonds are created; i.e., $n_{\rm b} \to n_{\rm b} + 2$ and $n_{\rm VB} \to n_{\rm VB} + 3$, but the number of vertices is unchanged, $n_{\rm v} \to n_{\rm v}$. $\Delta E_{i\to j}$ includes the binding energy of the two newly formed bonds, the two bending energies along the two newly bound edges and the stretching energy of the newly inserted subunit.

2. *Wedge removal*

The reverse move of wedge insertion is wedge removal. In a wedge removal, we randomly choose one of the removable wedges from a given structure. With the number of removable wedges as $n_{\rm wr}$, the attempt probability is

$$\alpha(j \to i) = n_{\rm wr} k_{\rm i} \tau \times \frac{1}{n_{\rm wr}}. \tag{20}$$

Using Eq. (18), the acceptance probability for a wedge removal is then

$$p_{\rm acc}(j \to i) = \min\left[1, \frac{\lambda^9}{v_{\rm a}^3} \exp[-(\Delta E_{j\to i} + \mu)/k_{\rm B}T]\right]. \tag{21}$$

We have the following constraints on rates $k_{\rm i}$ for wedge insertion/removal:

$$n_{\rm w} k_{\rm i} \tau n_{\rm r} < 1 \tag{22}$$

$$n_{\rm wr} k_{\rm i} \tau < 1 \tag{23}$$

As for simple insertion and removal, in the case of multiple species, detailed balance is satisfied for each species separately for wedge insertion/removal.

D. Wedge fusion / fission

1. *Wedge fusion*

In this move, a *fusable wedge* is closed, without inserting a new subunit (Fig 6). That is, the two vertices on either side of the wedge opening are merged into a single vertex. Fusable wedges are vertex pairs that i) form a wedge (as in the case of wedge insertion) and ii) are within a separation distance of $l_{\rm fuse}$.

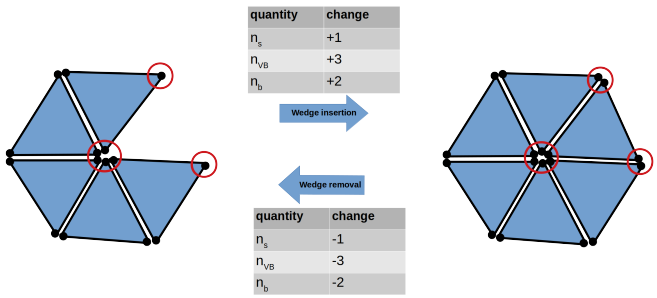

FIG. 5. Wedge insertion and removal.

Denoting the number of fusible wedge positions as $n_{\rm w}$, in each MC step, a wedge fusion is attempted with probability $n_{\rm w}k_{\rm wf}\tau$, where $k_{\rm wf}$ is an adjustable parameter controlling the relative probability of attempting wedge fusion. Then, a wedge position is selected randomly from the set of all $n_{\rm w}$ fusible wedges. The attempt probability is thus

$$\alpha(i\to j) = n_{\rm w}k_{\rm wf}\tau \times \frac{1}{n_{\rm w}}. \tag{24}$$

Using Eqs. (24) and (26), the acceptance probability for fusion moves is

$$p_{\rm acc}(i\to j) = \min\left[1, \frac{v_{\rm a}}{v_{\rm fuse}}\exp(-\Delta E_{i\to j}/k_{\rm B}T)\right] \tag{25}$$

where $v_{\rm fuse} = (4\pi/3)(l_{\rm fuse}/2)^3$ is the volume of a sphere with diameter $l_{\rm fuse}$, and $\Delta E_{i\to j}$ is the energy change due to the fusion, including changes in bending, stretching, and binding energies. A fusion move increases the number of edge bonds and vertex bonds by one, $n_{\rm b}\to n_{\rm b}+1$ and $n_{\rm VB}\to n_{\rm VB}+1$; the factor of $v_{\rm a}$ appears in Eq. (25) to account for the latter.

2. *Wedge fission*

Wedge fission, in which a wedge is opened, is the reverse of the wedge fusion move. Fissionable edges are those edges that can be split along their boundary vertex to obtain a wedge. Denoting the number of such edges as $n_{\rm f}$, the probability of attempting a wedge fission move during an MC step is $n_{\rm f}k_{\rm wf}\tau$. If a fission move is attempted, then an edge is selected randomly from the $n_{\rm f}$ fissionable edges. The position of one of the new vertices is selected randomly within the sphere of volume $v_{\rm fuse}$ centered at the original position of the merged vertices, and the other new vertex is placed in the opposite direction from the original position, at the same distance. Thus, the attempt generation probability is

$$\alpha(j\to i) = n_{\rm f}k_{\rm wf}\tau \times \frac{1}{n_{\rm f}(v_{\rm fuse}/{\rm d}\vec{x})} \tag{26}$$

and the acceptance probability is

$$p_{\rm acc}(j\to i) = \min\left[1, \frac{v_{\rm fuse}}{v_{\rm a}}\exp(-\Delta E_{j\to i}/k_{\rm B}T)\right] \tag{27}$$

We verify that detailed balance holds between wedge fusion and fission as follows. There are two cases to consider:

1. $(v_{\rm fuse}/v_{\rm a})\exp(-\Delta E_{j\to i}/k_{\rm B}T) < 1 \Leftrightarrow (v_{\rm a}/v_{\rm fuse})\exp(-\Delta E_{i\to j}/k_{\rm B}T) > 1$
   In this case, $p_{\rm acc}(i\to j) = 1$ and $p_{\rm acc}(j\to i) = (v_{\rm fuse}/v_{\rm a})\exp(-\Delta E_{j\to i}/k_{\rm B}T)$. Then

$$P_i \times \alpha(i\to j) \times p_{\rm acc}(i\to j) = \frac{1}{Z_\Omega} v_{\rm a}^{n_{VB,i}}\exp[-(E_i-\mu n_{s,i})/k_{\rm B}T]\frac{1}{\lambda^{9n_{s,i}}} \times {\rm d}^{\rm n_{v,i}}\vec{x} \times k_{wf}\tau \tag{28}$$

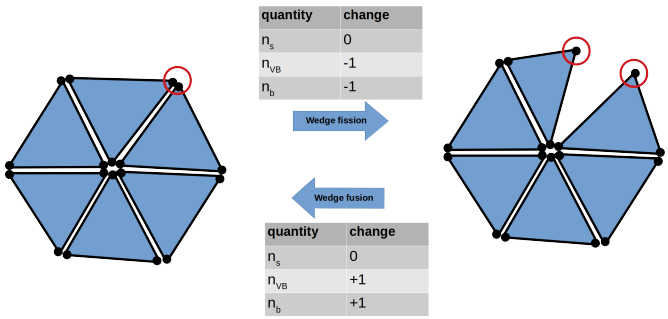

FIG. 6. Wedge fusion and fission.

and

$$P_j \times \alpha(j \to i) \times p_{\rm acc}(j \to i) = \frac{1}{Z_\Omega} v_{\rm a}^{n_{VB,j}} \exp[-(E_j - \mu n_{s,j})/k_{\rm B}T] \frac{1}{\lambda^{9n_{s,j}}} \times {\rm d}^{\rm n_v,j}\vec{x} \tag{29}$$

$$\times\, k_{wf}\tau {\rm d}\vec{x}/v_{\rm fuse} \times (v_{\rm fuse}/v_{\rm a}) \exp(-\Delta E_{j\to i}/k_{\rm B}T) \tag{30}$$

Using: $\Delta E_{j\to i} = E_i - E_j$, $n_{s,i} = n_{s,j}$ (because the move leaves the subunit number unchanged), $n_{VB,i} = n_{VB,j} - 1$ (one vertex bond is broken upon fission) and $n_{v,i} = n_{v,j} + 1$ (an extra vertex is being born upon fission), we see that the two are equal and detailed balance holds.

2. $(v_{\rm fuse}/v_{\rm a}) \exp(-\Delta E_{j\to i}/k_{\rm B}T) > 1 \Leftrightarrow (v_{\rm a}/v_{\rm fuse}) \exp(-\Delta E_{i\to j}/k_{\rm B}T) < 1$

In this case, $p_{\rm acc}(i \to j) = (v_{\rm a}/v_{\rm fuse}) \exp(-\Delta E_{i\to j}/k_{\rm B}T)$ and $p_{\rm acc}(j \to i) = 1$. Then

$$P_i \times \alpha(i \to j) \times p_{\rm acc}(i \to j) = \frac{1}{Z_\Omega} v_a^{n_{VB,i}} \exp[-(E_i - \mu n_{s,i})/k_{\rm B}T] \frac{1}{\lambda^{9n_{s,i}}} \times {\rm d}^{\rm n_v,i}\vec{x} \times k_{wf}\tau \tag{31}$$

$$\times\, (v_{\rm a}/v_{\rm fuse}) \exp(-\Delta E_{i\to j}/k_{\rm B}T) \tag{32}$$

and

$$P_j \times \alpha(j \to i) \times p_{\rm acc}(j \to i) = \frac{1}{Z_\Omega} v_a^{n_{VB,j}} \exp[-(E_j - \mu n_{s,j})/k_{\rm B}T] \frac{1}{\lambda^{9n_{s,j}}} \times {\rm d}^{\rm n_v,j}\vec{x} \tag{33}$$

$$\times\, k_{wf}\tau {\rm d}\vec{x}/v_{\rm fuse} \tag{34}$$

Using again $\Delta E_{j\to i} = E_i - E_j$, $n_{s,i} = n_{s,j}$, $n_{VB,i} = n_{VB,j} - 1$ and $n_{v,i} = n_{v,j} + 1$, detailed balance holds.

Note that detailed balance is satisfied regardless of the values of $k_{\rm wf}\tau$ or $v_{\rm fuse}$, but as with all of the move frequencies these parameters can be optimized during burn-in to accelerate convergence to the equilibrium distribution $P(i)$. In our simulations, we find that the optimal value of $v_{\rm fuse}$ is on the order of the optimal value of $d_{\rm max}$ for analogous reasons: if $v_{\rm fuse}$ is too small there will be very few vertex pairs identified as fusable, so $n_{\rm w}$ will be low. If $v_{\rm fuse}$ is too large, there will be many fusion candidates but most fusion attempts will be rejected due to the large elastic energy change necessary for the merging deformation.

Most importantly, we note the constraint on the parameters $k_{\rm wf}\tau$ to ensure that generation probabilities do not become larger than unity. Because each attempt is generated as a three step process, using three probabilities, one has to ensure that all those probabilities are less than 1. Specifically,

$$n_{\rm w} k_{\rm wf}\tau < 1 \tag{35}$$

$$n_{\rm f} k_{\rm wf}\tau < 1. \tag{36}$$

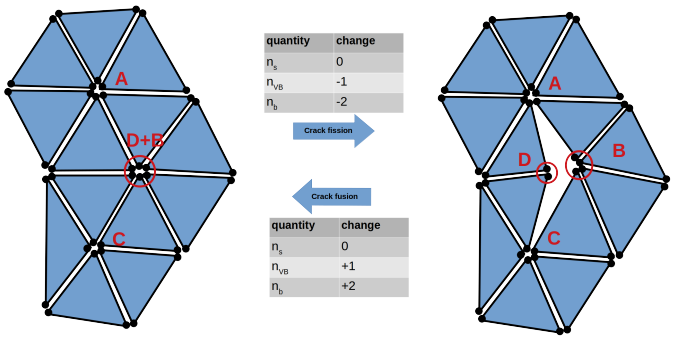

FIG. 7. Crack fusion and fission.

E. Crack fusion / fission

1. *Crack fusion*

Crack fusion closes a crack within the structure; i.e., two adjacent pairs of edges are merged (Fig. 7). Cracks are identified as 4-edge-length holes inside the structure. If the vertices of the hole are labeled A, B, C, D then the polygon ABCD forms a closed loop (see Fig. 7). The crack can be closed by either merging vertices A and C (and correspondingly edges CD to DA and AB to BC) or by merging vertices B and D (and correspondingly edges AD to AB and CD to CB). Each 4-edge-length loop thus defines two potential fusable cracks. However, an additional condition for a crack to be fusable is that its merging vertices must be within a distance l_{fuse} (A and C or D and B in this example). In this work, we have set the crack fusion volume to be the same as that for wedge fusion to reduce the number of parameters, but it is not necessary that they be the same.and the acceptance probability is

$$p_{\text{acc}}(i \to j) = \min\left[1, \frac{v_{\text{a}}}{v_{\text{fuse}}} \exp(-\Delta E_{i\to j}/k_{\text{B}}T)\right] \tag{37}$$

There are two edge bonds and one vertex bond formed during a crack fusion.

2. *Crack fission*

The reverse move for crack fusion is crack fission. With the number of potential cracks as n_{cf}:

$$\alpha(j \to i) = n_{\text{cf}} k_{\text{cf}} \tau \times \frac{1}{n_{\text{cf}}(v_{\text{fuse}}/\mathrm{d}\vec{x})} \tag{38}$$

$$p_{\text{acc}}(j \to i) = \min\left[1, \frac{v_{\text{fuse}}}{v_{\text{a}}} \exp(-\Delta E_{j\to i}/k_{\text{B}}T)\right] \tag{39}$$

As for the case of wedge fusion/fission, the crack fusion attempt frequency parameter k_{cf} is constrained by the conditions maintaining probabilities smaller than unity:

$$n_{\text{c}} k_{\text{cf}} \tau < 1 \tag{40}$$

$$n_{\text{cf}} k_{\text{cf}} \tau < 1 \tag{41}$$

$$\tag{42}$$

F. Edge fusion / fission

1. *Edge fusion*

During this move two non-neighbor edges are fused (Fig. 8). Fusable edges are non-neighboring edge pairs whose corresponding vertices are within a separation distance l_{fuse}. Since edges are directed, they can only fuse such that,

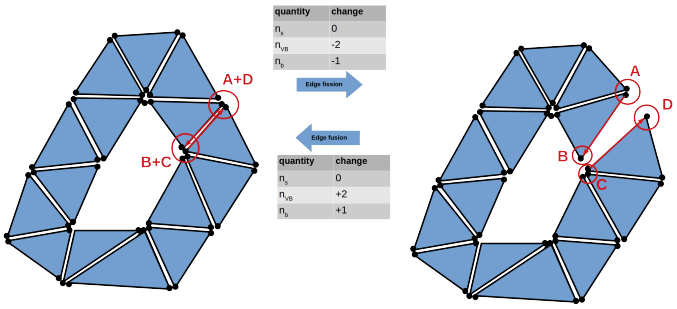

FIG. 8. Edge fusion and fission.

after fusion, they point in the opposite direction. Assuming the edges to be fused are $A \to B$ and $C \to D$ (see Fig. 8), vertex A will merge into vertex D and vertex B will merge into vertex C. Edges are counted as fusable if A is within a distance l_{fuse} to D and B is also within a distance l_{fuse} to C. The attempt probability is analogous to that for wedge and crack fusion/fission,

$$\alpha(i \to j) = n_{\text{e}} k_{\text{ef}} \tau \times \frac{1}{n_{\text{e}}} \tag{43}$$

with n_{e} the number of fusable edges and k_{ef} the edge fusion frequency parameter. The acceptance probability is

$$p_{\text{acc}}(i \to j) = \min\left[1, \left(\frac{v_{\text{a}}}{v_{\text{fuse}}}\right)^2 \exp(-\Delta E_{i\to j}/k_{\text{B}}T)\right] \tag{44}$$

During edge fusion, one edge bond and two vertex bonds are created.

2. *Edge fission*

Edge fission is the reverse move of edge fusion. n_{ef} is the number of breakable edges, that is, those edges that have both vertices on the boundary and which would not result in breaking the structure apart.

$$\alpha(j \to i) = n_{\text{ef}} k_{\text{ef}} \tau \times \frac{1}{n_{\text{ef}} (v_{\text{fuse}}/\mathrm{d}\vec{x})^2} \tag{45}$$

The factor $1/(v_{\text{fuse}})^2$ arises because we must select a random position for each pair of vertices, independently. The acceptance probability is then

$$p_{\text{acc}}(j \to i) = \min\left[1, \left(\frac{v_{\text{fuse}}}{v_{\text{a}}}\right)^2 \exp(-\Delta E_{j\to i}/k_{\text{B}}T)\right]. \tag{46}$$

To maintain probabilities within unity, the edge fusion frequency parameter k_{ef} is constrained by

$$n_{\text{e}} k_{\text{ef}} \tau < 1 \tag{47}$$

$$n_{\text{ef}} k_{\text{ef}} \tau < 1. \tag{48}$$

III. UMBRELLA SAMPLING, PARALLEL TEMPERING, AND FREE ENERGY CALCULATIONS

1. *Bias potentials.*

The grand potential (up to an n-independent constant $k_{\text{B}}T \ln Z_\Omega$), Ω_n, can be computed as $\Omega_n = -k_{\text{B}}T \ln P(n)$ where $P(n)$ is the equilibrium probability of observing n subunits in the structure. While $P(n)$ can in principle be computed by tabulating a histogram of cluster sizes during an unbiased simulation, in practice only the high-probability

cluster sizes will result in statistically significant sampling. To improve sampling, we perform umbrella sampling, with independent windows in which a harmonic bias potential $U_{\rm b} = k_{\rm umbrella}(n-n_0)^2/2$ that restrains the cluster size to remain near n_0, with $k_{\rm umbrella}$ the strength of the bias potential, and each window can have different values of n_0 and $k_{\rm umbrella}$. We perform simulations in which histograms corresponding to the biased probability distribution $P_{\rm bias}(n)$ are measured; the biased histograms are then combined and unbiased using the Weighted Histogram Analysis Method [7] to obtain Ω_n. We used the Bayes-WHAM implementation by Ferguson [8].

The interaction free energy F_n is then given by $F_n = \Omega_n + \mu n$, with μ the chemical potential. Importantly, measurements performed at different chemical potentials μ should result in the same F_n, since F_n represents the cluster interaction free energy which is independent of the bath concentration. However, different imposed values of μ will 'tilt' the free energy landscape and thus favor sampling different values of n for a given bias potential. Therefore, it is useful to combine the imposed chemical potential into the bias potential as:

$$U_{\rm b}(n, n_0) = k_{\rm umbrella}\frac{(n-n_0)^2}{2} - \mu(n-n_0) \tag{49}$$

The n_0 in the linear term does not affect the computed value of F_n (which depends only on $\partial U_{\rm b}/\partial n$) but is convenient for numerical reasons in solution of the WHAM equations. The simulation is then performed with a Hamiltonian $H(\Gamma) = E(\Gamma) + U_{\rm b}(n, n_0)$.

2. Parallel tempering

Convergence of umbrella sampling calculations is poor when there are slow degrees of freedom in addition to reaction coordinate being biased (which is the cluster size n in our case). Moreover, because our reaction coordinate is discrete, sampling may be poor in cases where the underlying free energy landscape has a jump which is large in comparison to $k_{\rm B}T$ over a single subunit. Therefore, to improve sampling, we performed parallel tempering between different umbrella sampling windows and replicas at different temperatures. In particular, we simultaneously performed simulations with 3 different temperatures, 4 umbrella spring constants $k_{\rm umbrella}$ and 3 chemical potentials μ (36 replicas in total). Swaps between these replicas were attempted randomly, with the Metropolis acceptance criteria to ensure detailed balance ([6]). In principle, results from all of these windows could be combined within WHAM, but in practice combining different temperatures is impractical for a histogram-based method such as WHAM and instead requires use of 'binless' WHAM (e.g. [9, 10]). Therefore, we separately used WHAM to compute free energy profiles at each of the three temperatures. For the results in the main text, each free energy curve (and corresponding minimum point) result from exchanging between 36 replicas with $k_{\rm B}T = \{1, 1.1, 1.25\}$, $\mu = \{-6.5, -5.5, -5\}$, $k_{\rm umbrella} = \{1, 1.5, 2, 2.5\}$. Technically, a non-unit temperature is equivalent to rescaling the elastic moduli, binding energies, chemical potential and the umbrella spring constant by the same factor, however, it is easier to implement with having the temperature as a separate parameter.

IV. MAPPING TO TARGET CURVATURES FROM LOCAL DIHEDRALS

Here we briefly outline the mapping between preferred dihedrals between adjacent triangular edges and the *target* values for target (triangulated) surface. Notably, the target shape prefers a non-zero Gaussian curvature that is incompatible with the equilateral edge lengths, and hence, we deduce the values of the target curvature from *unfrustrated strips* along nearest neighbor rows of triangles. Consider for example, a row shown in Fig. 9(a) corresponding to an alternating sequence of dihedrals, θ_i and θ_j. The curvature along this row is defined by considered the circle defined by three consecutive vertices along the row, see the green, blue and yellow points in Fig. 9(a) . These points define a vector $\mathbf{R}(\theta_i, \theta_j)$ that points from the central vertex to the center of curvature, such that the local radius of curvature is its length. As the local discrete approximation to the curvature of these edges is $\mathbf{R}(\theta_i, \theta_j)/|\mathbf{R}(\theta_i, \theta_j)|^2$, the discrete approximation of the *normal curvature* of a surface spanned by the triangular faces is given by,

$$\kappa(\theta_i, \theta_j) = \frac{\mathbf{n}\cdot\mathbf{R}(\theta_i, \theta_j)}{|\mathbf{R}(\theta_i, \theta_j)|^2} = \frac{2\sqrt{3}(\sin\theta_i + \sin\theta_j)\big(\cos\theta_i + \cos\theta_j + \cos\theta_i\cos\theta_j - 2\sin\theta_i\sin\theta_j - 3\big)}{\ell_0\big[4\cos\theta_i + 4\cos\theta_j - 8\cos(\theta_i - \theta_j) + 3\cos(2\theta_i) + 3\cos(2\theta_j) - 6\big]} \tag{50}$$

where $\mathbf{n}$ is the normal to the central triangle, and ℓ_0 is the preferred edge length. For small angles this row curvature reduces to the simple form

$$\kappa(\theta_i \ll 1, \theta_j \ll 1) \simeq \frac{\sqrt{3}(\theta_i + \theta_j)}{2\ell_0}. \tag{51}$$

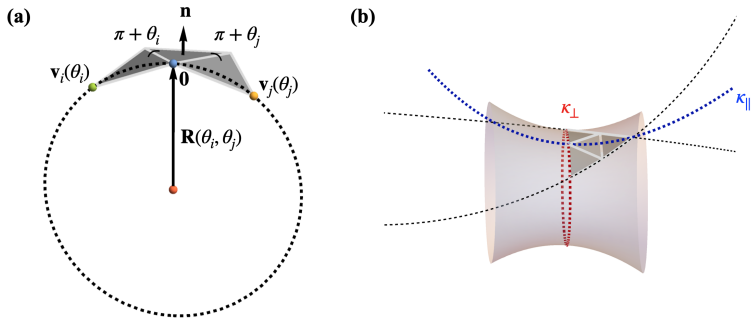

FIG. 9. Schematic for defining target curvatures from preferred dihedrals of triangular subunits. (a) shows the definition of target curvature along a row of triangles with consecutive dihedrals, θ_i and θ_j, based on the circle defined by 3 consecutive vertices, shown as green, blue, and yellow points. The vectors $\mathbf{R}(\theta_i, \theta_j)$ and $\mathbf{n}$ denote the distance from the central vertex to the center of curvature and the normal to the triangular face, respectively. (b) shows a schematic relating the two target principle curvatures, $\kappa_\perp$ and $\kappa_\parallel$, to the row curvatures of the triangular mesh, one of which lies along the principle $\perp$ direction, while the other two are shown as the dashed black curves.

Based these row curvatures, we can relate them to the principle curvatures $\kappa_\parallel$ and $\kappa_\perp$ using Euler's relation,

$$\kappa(\theta_i, \theta_j) = \kappa_\parallel(\hat{\mathbf{e}}_\parallel \cdot \hat{\mathbf{e}}_{ij})^2 + \kappa_\perp(\hat{\mathbf{e}}_\perp \cdot \hat{\mathbf{e}}_{ij})^2, \tag{52}$$

where $\hat{\mathbf{e}}_\parallel$ and $\hat{\mathbf{e}}_\perp$ are the principle directions of curvature and $\hat{\mathbf{e}}_{ij}$ is the direction of the row of alternating ij bonds in the tangent plane. For trumpets, the dihedrals in the hoop ($\perp$) direction are equal to a common θ_2, such that

$$\kappa_\perp = \kappa(\theta_2, \theta_2), \tag{53}$$

while the directions of the θ_1 and θ_2 are rotated by $2\pi/3$ with respective to this principle direction giving,

$$\kappa_\parallel = \frac{4\kappa(\theta_2, \theta_1) - \kappa(\theta_2, \theta_2)}{3}. \tag{54}$$

This alignment of the target row curvatures and principle curvature directions is shown schematically in Fig. 9(b).

[1] Grant M. Rotskoff and Phillip L. Geissler. Robust nonequilibrium pathways to microcompartment assembly. *Proceedings of the National Academy of Sciences of the United States of America*, 115(25):6341–6346, 2018.

[2] Christian Sigl, Elena M. Willner, Wouter Engelen, Jessica A. Kretzmann, Ken Sachenbacher, Anna Liedl, Fenna Kolbe, Florian Wilsch, S. Ali Aghvami, Ulrike Protzer, Michael F. Hagan, Seth Fraden, and Hendrik Dietz. Programmable icosahedral shell system for virus trapping. *Nature Materials*, 2021.

[3] Michael F. Hagan, Oren M. Elrad, and Robert L. Jack. Mechanisms of kinetic trapping in self-assembly and phase transformation. *Journal of Chemical Physics*, 135(10):1–13, 2011.

[4] Michael F. Hagan and David Chandler. Dynamic pathways for viral capsid assembly. *Biophysical Journal*, 91(1):42–54, 2006.

[5] M Botsch, S Steinberg, S Bischoff, and L Kobbelt. OpenMesh – a generic and efficient polygon mesh data structure. In *OpenSG Symposium*, 2002.

[6] Daan Frenkel and Berend Smit. Understanding molecular simulation: From algorithms to applications, 1996.

[7] Shankar Kumar, Djamal Bouzida, Robert H. Swendsen, Peter A. Kollman, and John M. Rosenberg. The weighted histogram analysis method for free-energy calculations on biomolecules. *Journal of computational chemistry*, 13(8):1011–1021, 1992.

[8] Andrew L. Ferguson. BayesWHAM: A Bayesian approach for free energy estimation, reweighting, and uncertainty quantification in the weighted histogram analysis method. *Journal of Computational Chemistry*, 38(18):1583–1605, 2017.

[9] Zhiqiang Tan, Junchao Xia, Bin W. Zhang, and Ronald M. Levy. Locally weighted histogram analysis and stochastic solution for large-scale multi-state free energy estimation. *Journal of Chemical Physics*, 144(3):40–44, 2016.

[10] Zhiqiang Tan, Emilio Gallicchio, Mauro Lapelosa, Ronald M Levy, Zhiqiang Tan, Emilio Gallicchio, Mauro Lapelosa, and Ronald M Levy. Theory of binless multi-state free energy estimation with applications to protein-ligand binding Theory of binless multi-state free energy estimation with applications to protein-ligand binding. *Journal of Chemical Physics*, 0341070341:1–14, 2012.